Thin-Walled Structures 186 (2023) 110661

Contents lists available at ScienceDirect

Thin-Walled Structures

journal homepage: www.elsevier.com/locate/tws

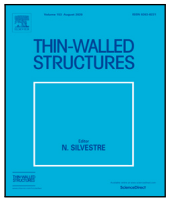

Full length article

Experimental and numerical study of structural damping in a beam with bolted splice connection

O. Mijatović [a,b], A. Borković [a,c,*], M. Guzijan-Dilber [d], Z. Mišković [b], R. Salatić [b], R. Mandić [b], V. Golubović-Bugarski [e]

[a] University of Banja Luka, Faculty of Architecture, Civil Engineering and Geodesy, Department of Mechanics and Theory of Structures, Bulevar Vojvode Stepe Stepanovića 77/3, 78000 Banja Luka, Bosnia and Herzegovina
[b] Faculty of Civil Engineering, University of Belgrade, Bulevar kralja Aleksandra 73, 11000 Belgrade, Serbia
[c] Institute of Applied Mechanics, Graz University of Technology, Technikerstraße 4/II, 8010 Graz, Austria
[d] Peter the Great St. Petersburg Polytechnic University, Polytechnicheskaya 29, 195251, St. Petersburg, Russia
[e] University of Banja Luka, Faculty of Mechanical Engineering, Bulevar Vojvode Stepe Stepanovića 71, 78000 Banja Luka, Bosnia and Herzegovina

ARTICLE INFO

Keywords:
Bolted beam splice connection
Nonlinear dynamic analysis
Structural damping
Frictional contact

ABSTRACT

The objective of this research is to develop a numerical model of one widely used bolted beam splice connection that dissipates energy through structural damping. The reference experimental setup is carefully designed to obtain the highly nonlinear dynamic response due to the suddenly released load. The fact that the monolithic beam with welded connection has a linear response is utilized for the initial calibration of the numerical and experimental models. Then, the numerical model of bolted beam splice connection is verified and adopted through an iterative process. The influences of time and spatial integration, bolt load application, element type, contact formulation, bulk viscosity, and mass scaling are discussed. A special attention is given to the load application and load release functions. After the verification, the Abaqus/Explicit numerical model is validated through the comparison with experimental data, where an appropriate friction coefficient is adopted. It is demonstrated that the nonlinear structural damping occurs due to the complex micro slip behavior at the contact interface.

1. Introduction

The design of modern steel and aluminum structures requires various mechanical connections. One of the most prominent types of these mechanical joints is the bolted splice connection (BSC), designed by introducing a large compression force between the elements in contact interaction. The basic function of a BSC is to connect two elements and to allow the force transfer between them. The mechanical behavior of these joints plays an important role in the overall dynamic response of complex engineering structures. Eigenmodes of vibration and nonlinear structural response heavily depend on contact interactions in BSCs. For example, the stress distribution and slip/stick phenomena in joints can affect the stiffness, plasticity, and frictional damping [1]. Therefore, a great amount of existing research is dedicated to the development of accurate, general, and efficient computational and experimental models of structures with mechanical connections and interfaces [2,3].

Different types of mechanical connections are displayed in Fig. 1. The connection shown in Fig. 1a represents a basic scheme of the BSC with its stick, slip and opening regions. Due to the bolt tightening force, the stick region exists near the bolt shank while the slip occurs near the perimeter of the washer. Further away from the washer, the contact pressure decreases while the relative displacement between joined elements increases. This can be followed by the opening, where the contact pressure and slip vanish. Fig. 1b shows a bolted beam splice connection (BBSC), which is one of the most common connections in structural engineering. Furthermore, the various BSCs that are predominantly used in the aviation industry are displayed in Fig. 1c. The fir-tree connections between turbine blades and the mounting disc are shown in Fig. 1d. They require special attention due to the complexity of the wear, damage, and energy dissipation processes [6,7].

The standard numerical approach for the analysis and design of mechanical connections is the finite element (FE) method [8–10]. It can estimate eigenmodes and system response, therefore allowing engineers to design with respect to a given criterion and material properties. One of the remaining challenges is to implement uncertainties of geometric and material properties of the BSC contact interactions in the FE codes. This leaves the problem of accurate and efficient modeling of BSCs

* Corresponding author at: University of Banja Luka, Faculty of Architecture, Civil Engineering and Geodesy, Department of Mechanics and Theory of Structures, Bulevar Vojvode Stepe Stepanovića 77/3, 78000 Banja Luka, Bosnia and Herzegovina.
E-mail addresses: aleksandar.borkovic@aggf.unibl.org, aborkovic@tugraz.at (A. Borković).

https://doi.org/10.1016/j.tws.2023.110661
Received 14 September 2022; Received in revised form 5 February 2023; Accepted 24 February 2023
Available online 4 March 2023

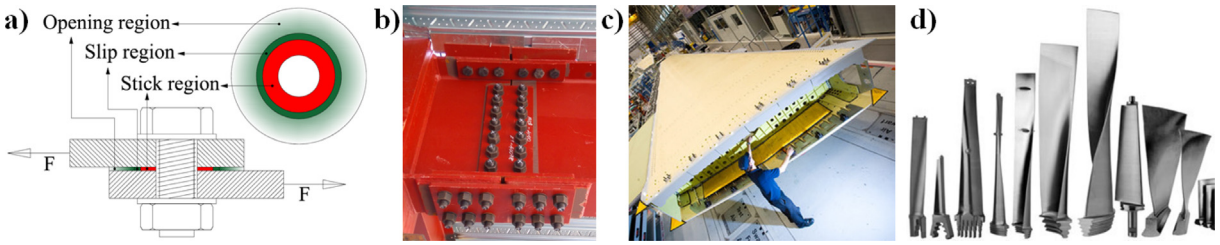

Fig. 1. Typical mechanical connections: (a) the simple overlap connection with stick, slip and opening regions, (b) the bolted beam splice connection in steel structures, (c) the splice connection in the aviation industry [4], (d) turbine blades with fir-tree connections [5].

during the nonlinear dynamic response still open. The main issue is the modeling of structural damping, which is the prevailing mechanism of energy dissipation in jointed structures. Structural damping strongly affects the dynamic response and eigenmodes, making the problem of jointed structures highly nonlinear. Despite its utmost importance, this phenomenon is yet to be well-understood.

Structural damping of jointed structures largely depends on the properties of surfaces in contact interactions and on the activation of stick/slip regions during the dynamic response. As the structure gets excited, a relative motion between surfaces in contact initially occurs across small regions of contact interface, while the majority of contact surfaces stays fixed with respect to each other. The areas where these states exist are defined as the slip and the stick regions, respectively. The phenomenon of relative motion over small regions of contact interface is designated as the micro slip. As the intensity of excitation force increases, the slip region increases as well. If the excitation exceeds a threshold value, the slip occurs across the entire contact interface and this phenomenon is known as the macro slip [11–13]. A well-designed bolted connection prevents macro slip, but some micro-slipping is always present in real-life working conditions [2,3].

Let us briefly discuss some of the main factors that influence contact interaction. The problem is more complex than the pure friction described by Coulomb's law and the friction coefficient [14–16]. Additional parameters are material change, plastification, and degradation [16,17]. These are followed by unpredictable changes in the total real contact area involved in the interaction [18] and by changes in stick/slip conditions [19,20]. Another important property is the surface roughness, which is crucial for some engineering applications. For the definition of contact geometry, Greenwood–Williamson's and Persson's models are readily used [21–23]. The contact geometry and separation are highly nonlinear, and their numerical solution requires a massive computational algorithm [24,25]. Therefore, an accurate modeling of contact geometry is a challenging task, whether with experimental, analytical, or numerical approaches [16,17,19,20,26–32]. The complexity of contact modeling increases with a decrease in scale while gaining further insight into its real nature. The contact interaction of two general bodies at an atomic or nano-level is a multi-physical problem where several scientific disciplines intertwine [33].

It is fascinating that practically all surfaces found in nature have roughness, with the exception of some unique materials such as mica, which has a smooth molecular surface [34]. Segalman and Brake investigated the influence that contact surface roughness, as a micro scale quantity, has on the overall macro response of a bolted connection [2,3,35]. In these studies, the authors emphasize the contact roughness influence on the jointed structure response and on contact pressure distribution. Furthermore, Fantetti et al. examined the dry friction between two stainless steel wedges with a contact interaction surface of only 1 mm^2 [36]. Despite the extremely small contact area, the change of roughness in contact surfaces due to the sliding friction caused a significant change in the eigenmodes of the complete experimental setup that had a weight of 22.4 kg! This experiment clearly indicates the substantial influence that roughness has on dynamic response.

When we limit the research to dry friction and aim to compare numerical and experimental results, we should consider what dry friction actually is, and whether and in what way it is possible to achieve ideally dry and clean metal surfaces without the influences of oxides and humidity [17,37,38]. It is remarkable that even an apparently trivial phenomenon, such as air humidity, can significantly affect the friction in joints [39,40], and thus, structural damping. Also, oxides and their formation time considerably influence the friction in mechanical connections [16,17,41]. The physical and mechanical characteristics of the oxide and its effect on the friction and overall response of the jointed structures are yet to be fully understood [17,42]. Various experimental procedures have shown that, after the oxide thickness exceeds the limit of 5–10 nm, the friction between steel surfaces reduces due to adhesion reduction [43–45]. For very clean, smooth surfaces and for tests performed in a vacuum immediately after cleaning, it has been found that the friction can increase by several orders of magnitude [41,46–48]. Furthermore, during the high frequency micro- and macro-slipping under large pressure, the micro asperities yield and melt, which requires a proper thermodynamical formulation and further complicates the dry friction contact modeling. A process of the local heating and melting of micro asperities is known as *flash-heating*, and it reduces friction [49–51].

Besides the aforementioned phenomena that are mostly related to dry friction, let us note additional parameters that affect friction in general: type of material [52–54], lubrication and presence of different fluids [55–57], and changes in the material phase and structure caused by heating or radiation [58]. Again, this brief review of the main parameters that influence contact interactions reveals why the modeling of connections in engineering structures is an active and challenging research area. In essence, the impact that processes at the nano and atomic levels have on the macro scale system response perplexes the accuracy and efficiency of mechanical models [34,59].

Segalman discussed the lack of proper understanding of jointed structures [2]. Twenty researchers were asked: "How do you model jointed connections?" It was found that there were more ways to describe mechanical connections than there were survey participants. Hence, there is no uniform solution or agreement when it comes to the computational modeling of mechanical connections and structural damping. However, one can distinguish between three main approaches to the study of joint dynamics. The first approach is to define the exact physics of interactions inside the bolted connection starting from the micro scale and to consider a variety of uncertainties related to the description of surfaces that come in contact. The second approach is to investigate the joint dynamics at the macro scale, thus avoiding the description of micro scale surface geometry and the conditions of contacting parts. The objective of this approach is to investigate the dynamic response of the joint as a whole, and to identify crucial parameters that allow the prediction of structural response. Finally, there is a multi-scale approach that acquires data from the micro scale and applies it via appropriate parameters to the macro scale models.

Regarding the macro scale approach that is in the focus of our study, many different experimental and numerical methods exist [13,60–65]. Most of these methods are based on detailed experimental and numerical analyses of simple models. A detailed insight into the

nonlinear response of bolted joints is accomplished through a series of experiments and by the development of a numerical procedure using a four-parameter Iwan model [2,3,66–70]. The importance of scaling between the bolt tightening force and the excitation force magnitude is observed in these studies. When the disturbing force magnitude is small in relation to the bolt tightening force, the connection will not be activated. In other words, the size of the slip region inside the contact interaction will not reach a threshold value that triggers the nonlinear dynamic response and structural damping. If this is the case, the majority of the contact interaction is in the stick regime and only material damping will occur. For simple steel structures, such as beams and brackets, the material damping ratio is around 0.001 [2,3,63].

This brief review shows that contact in structural connections is a phenomenon that requires further investigation. The contact between two bodies and the process that takes place within the interaction of their contact surfaces can be classified as an exceedingly nonlinear dynamic problem for which no single and uniform solution exists [2,3,24,71,72]. Furthermore, the papers dealing with the structural damping in BBSCs are rare in the literature. Motivated by the importance and complexity of contact interactions for bolted structures, we have studied in detail one mechanical joint in this paper.

Accurate and efficient numerical modeling of one connection is a first and crucial step towards the final goal: the development of a numerical model that can predict energy dissipation of an overall structure. With this capability, we could improve the design process, assess structural health, detect early signs of wear, and prevent failure of a structure. Our research follows a macro scale approach and the secondary phenomena arising in bolted connections that can influence structural response. Some preliminary findings are already discussed in previous papers [73,74]. The main contributions of the presented research are the comprehensive calibration, verification, and validation of a numerical model of one BBSC. The experiment was carefully designed to trigger a significant nonlinear dynamic response of an IPE cantilever beam. For the initial verification and validation, we utilized a monolithic model with welded connection. Then, by a deliberate calibration of the Abaqus/Explicit numerical model, we obtained a reasonably accurate structural response. The adopted numerical model of BBSC allows an insight into the complex stick/slip state that is the main cause of structural damping.

The adopted numerical model has 69 contact pairs, which presents a complicated problem from the point of view of contact mechanics. Yet, from the point of view of structural engineering, this joint is a simple and widely-used connection. To bridge this gap, one must balance between the accuracy and the efficiency provided by available formulations and tools. For the present study, we have utilized several different hardware configurations, but the results are given for the reference configuration with i7-9700K CPU and 32 GB RAM.

The paper is organized as follows. The next section considers general remarks on the comparison of numerical and experimental results, required for the validation of our numerical model. The third section presents the experimental setup, results, and post-processing procedure. The calibration, verification, and validation of the numerical model are given in Section 4. The main findings and conclusions are discussed and summarized in the last two sections.

2. Experimental analysis

The experimental analysis consists of three steps: (i) design, preparation, and realization of the experimental testing, (ii) processing of the obtained data, and (iii) analysis of the results. These steps are discussed in detail in this section. In addition to the experimental model, an outlook towards the numerical model and its results is given. This kind of presentation is warranted since the numerical and experimental analyses are intertwined.

2.1. Preliminary remarks

Our analysis aims to develop and validate a numerical model via a comparison of the experimental and numerical results. The considered beam is a typical structural member with relatively small fundamental frequency due to added mass. Since the utilized load predominantly excites the fundamental mode of vibration, our study deals with a low-frequency response during a relatively long time interval. This profoundly affects the explicit nonlinear numerical analysis. Since the time increment of an explicit algorithm can be very small, the recording of results at every increment produces large output files and has high computational costs. The common solution is to calculate output variables at each n_{out} integration steps or each t_{out} intervals of time. However, this procedure can lead to aliasing issues that occur when a signal is sampled at discrete points, but not enough data points are saved to correctly describe the original signal [75,76]. The variables with high frequencies and large amplitudes, such as the accelerations and the reaction forces, are the most susceptible to aliasing [77]. The NASA Technical Memorandum [78] shows that even 10^4 outputs per second are not enough to avoid aliasing in drop test simulations. One method to mitigate aliasing is to apply an anti-aliasing filter, but such a procedure is not straightforward [79,80]. Another way to avoid these issues is to consider velocities that are significantly less sensitive to sampling rates and high-frequency noise. To enable consistent comparison of the experimental and numerical data, we have numerically integrated the experimental acceleration responses in cf. Section 2.4.1 and the velocity field is referenced almost exclusively. Furthermore, the outputs in our numerical model were taken every 0.00781 s, which corresponds to the sampling rate of 128 results per second. This rate is the same as in the experimental analysis, cf. Section 2.2.1. The time period considered with the numerical analysis was approximately 6.5 s. For the adopted numerical model, Abaqus required close to 53 h of computational time during which 3×10^7 increments were calculated.

2.2. Experimental setup

To enable a consistent comparison of the experimental and numerical results, it is necessary to properly define the experimental setup. This includes the design of connections and load, definition of the loading procedure, and design of the clamped boundary condition.

2.2.1. General considerations

The aim of the experimental analysis was to examine the nonlinear behavior of one IPE 80 beam with a commonly utilized BBSC. The free vibration response due to the suddenly released load was observed. To simulate real-life working conditions, the experiment was set up in the open, with relative air humidity of approximately 70%–80%. Although the focus of our research is on the model with a bolted connection, a model with a welded beam splice connection (WBSC) was considered as well. The free vibration response of such a beam is linear, making the WBSC model ideally suited as a reference for the calculation of the material damping and the initial calibration of the numerical model. A reasonable assumption is that the WBSC model represents the limit case of the BBSC model when the slip is negligible. In such a case, the bolted connection behaves as monolithic, see Section 4.

A detailed drawing and an image of the physical model are given in Fig. 2. At the free end, the beam had a fixed mass (M1) and an additional mass (M2). After a sudden removal of the additional mass, the beam entered the free vibration response. This additional mass was applied monotonically in increments of 25 kg. The additional mass was then released by cutting the attached wire that is 3 mm thick. In order to reduce the effect of wire cutting on the consistency of the experimental results, we have also tested wires that are 1.5 mm and 2 mm thick. However, the 3 mm wire was the thinnest one that could carry the additional mass. The 3 mm wire was near the yield point, so only a small damage was required for it to break. This approach is similar to

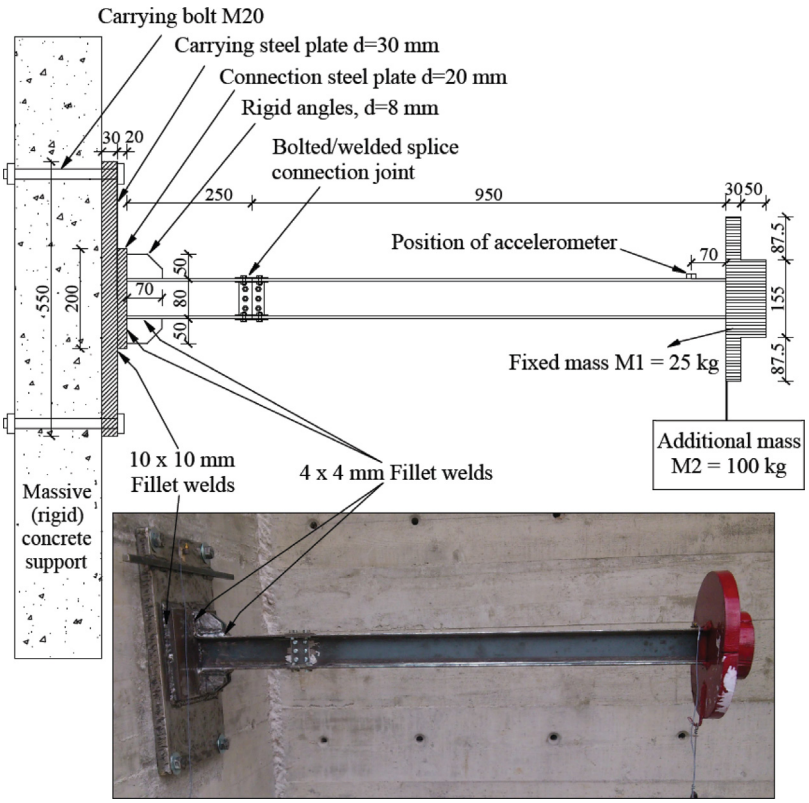

Fig. 2. Experimental setup. Detailed drawing and physical model.

the modeling of a suddenly released load by Pagnini in [81], where a specially designed test tube was calibrated to break after the load reaches the desired value.

The main subject of our study is the response of the BBSC model that is excited with respect to the major principal axes of inertia. Regarding the simple WBSC model, we have examined its response with respect to both principal axes of inertia, in order to estimate the influence of geometry on the material damping.

The free vibration response was measured with a one-axis accelerometer fixed near the free end, see Fig. 2. The accelerometer has a sensitivity of 96.6 mV/g and a frequency range of 0.3–6000 Hz. The sampling rate was set at 128 outputs per second, which is sufficient to capture the considered acceleration response.

2.2.2. Design of clamped boundary condition

One of the most important initial challenges was the design and construction of the clamped boundary condition. Failing to properly build the clamped end can result in parasitic vibrations due to the rotation of the connection plates. To define a physical model that can be constructed, we considered an initial numerical model. Additionally, a numerical model with an idealized fixed boundary condition was made. The main requirement for the calibration of the model with designed clamped end was the agreement between the fundamental frequencies of these two numerical models. The agreement is achieved through a variation of several approaches and parameters, and the adopted model was successfully constructed, see Fig. 2.

The beam was welded to a $200\times200\times20$ mm connection steel plate via rigid angles and 4×4 mm fillet welds, Fig. 2. This assembly was then welded to a carrying steel plate with dimensions $550\times350\times30$ mm. An approximate weld size between the connection and carrying steel plates is 10×10 mm. The oversized steel plates and welds were intentionally used to ensure an absolutely rigid connection between the beam and the carrying plate. Finally, the carrying plate was connected to a 300 mm thick concrete wall with four M20 bolts, as shown in Fig. 2. With such a construction, we achieved an almost ideally clamped boundary condition.

2.2.3. Model with the bolted beam splice connection

As discussed in the introduction, it is crucial to ensure the activation of micro slip regions in the connection to obtain the nonlinear response of the BBSC. Furthermore, to guarantee consistent results over all tested models, an initial macro slip had to be allowed during the application of the load. We achieved these requirements by means of a careful design of the connection with respect to the applied load.

The position of the connection was set at 250 mm from the clamped end. To simulate real-life working conditions, the static loading by the masses M1 and M2 was designed to utilize 50% of the elastic moment capacity of the observed section [82,83]. Since the BBSC model had been analyzed only with respect to the major principal axis, the required mass was adopted as 125 kg, of which the fixed mass was M1 = 25 kg and the additional M2 = 100 kg.

After defining the static loading, the BBSC was designed, see Figs. 2 and Fig. 3a. The connection consists of two $65\times46\times2$ mm outer flange splice plates and two pairs of $65\times18\times2$ mm inner flange splice plates. Additionally, the web splice plates are 62×50×2 mm. The tightening was achieved by four M8 bolts for the flanges and six M6 bolts for the webs. The grade of utilized bolts is 8.8, while the diameters of bolt holes are 10 mm and 8 mm for M8 and M6 bolts, respectively. The holes were designed to provide a 1 mm gap around the bolt's shank. Also, a 1 mm gap was left between the two parts of the beam that had been joined.

The BBSC model was tested for three levels of the bolt tightening force. The values of $M_r = 25$ Nm and $M_r = 10$ Nm were adopted as the maximum tightening torques for M8 and M6 bolts, respectively. These torques resulted in respective tightening forces of $F_p = 16$ kN and $F_p = 8$ kN [84,85], Table 1. The considered levels of bolt tightening forces were measured with respect to these maximum values. The appropriate models were designated as BBSC100, BBSC50, and BBSC30, and they refer to 100%, 50%, and 30% of the respective maximum tightening force.

These design choices satisfied the requirements for the nonlinear response and the consistent results across different models. The macro slip is anticipated for all models during the quasi-static application

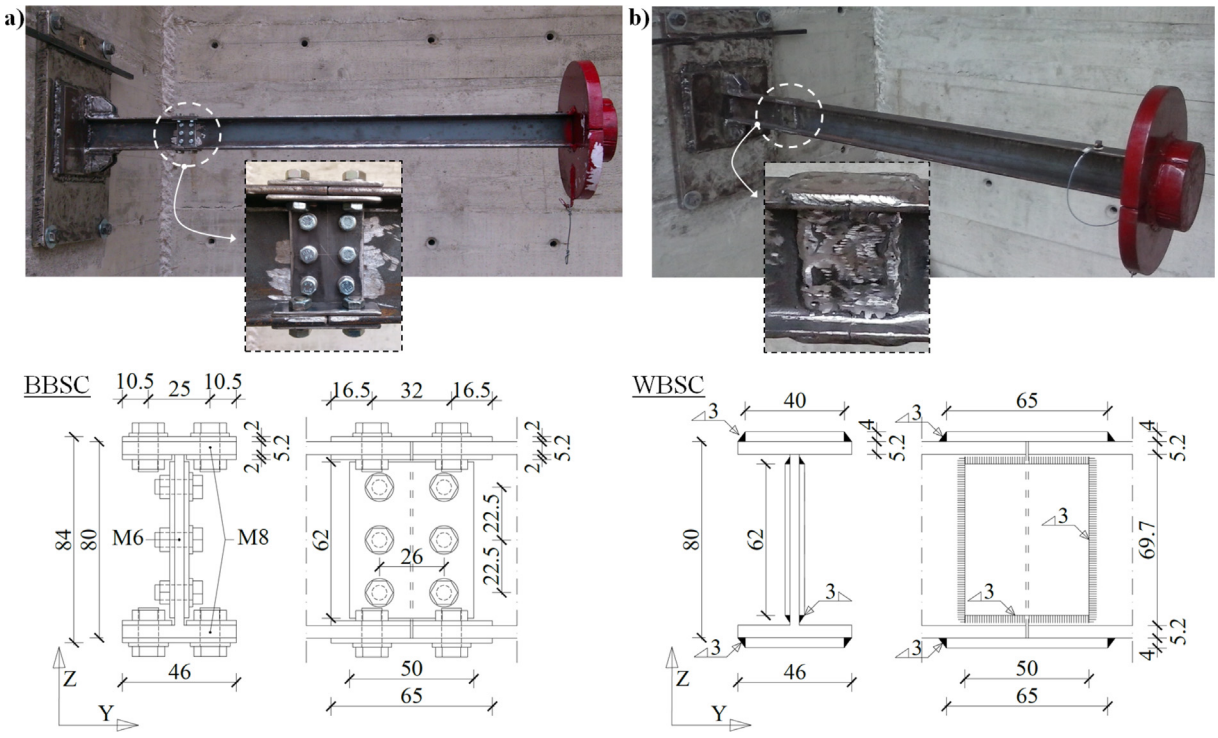

Fig. 3. Experimental setup. Images and detailed drawings of connections in physical models. (a) Bolted beam splice connection. (b) Welded beam splice connection.

Table 1
Approximate values of the bolt tightening forces for the three BBSC models.

Model	Tightening force M8 [kN]	Tightening force M6 [kN]	Percentage of maximum force [%]
BBSC100	16	8	100
BBSC50	8	4	50
BBSC30	5	2.5	30

of the additional mass, and the micro slip during the free vibration response. Furthermore, due to the allowed initial macro-slipping, a complex stress state is expected to arise in the connection.

2.2.4. Model with welded beam splice connection

The WBSC consists of two $65 \times 45 \times 4$ mm outer flange splice plates and two $62 \times 50 \times 2$ mm web splice plates. Let us note that the two flange splice plates at 2 mm thick are applied to the BBSC, while only one flange splice plate 4 mm thick is used for the WBSC. Nevertheless, the moment capacity of both connections is similar if the reduction of the cross-sectional area due to the bolt holes is neglected, Fig. 3b.

For the loading case with respect to the major principal axis, the masses are the same as for the BBSC: M1 = 25 kg and M2 = 100 kg. Regarding the loading case with respect to the minor principal axis, we have set a requirement that the maximum normal stresses due to the gravity should be close for both loading cases. Since the elastic section moduli with respect to the principal axes of the IPE 80 section are $W_{el,y} = 20.03$ cm^3 and $W_{el,z} = 3.69$ cm^3, the masses M1= 0 kg and M2= 25 kg are adopted for the case of bending with respect to the minor principal axis.

2.3. Experimental results

The experiment was based on the free vibration response approach. The acceleration time history was recorded and an auto spectrum response (ASR) was found via the Fast Fourier Transform [86–89]. The advantage of this approach is that a structure can be analyzed in real-life conditions. On the other hand, the free vibration response does not guarantee the excitation of all eigenmodes, in contrast to the experimental modal analysis in controlled conditions using the modal hammer. The number of recorded modes with the free vibration response analysis depends on the experimental setup, the number and positions of accelerometers, the load, etc. For the purpose of our analyses, the lowest bending mode that occurs in the plane of the load and the beam axis is of the most importance, and we refer to it as the *fundamental mode*.

The experimental acceleration time histories and the ASRs are presented in this subsection, along with the numerical results for the WBSC model.

2.3.1. Model with bolted beam splice connection

The measured acceleration time history responses and ASRs for the models with three different bolt tightening forces are displayed in Figs. 4 and 5. Evidently, the differences in the acceleration amplitudes across the models are significant and the values approximately follow the corresponding tightening force. For example, during the initial 0.5 s, the difference between BBSC100 and BBSC50 is nearly 50%. Next, the difference in amplitudes between BBSC100 and BBSC50 is more pronounced than the difference between BBSC50 and BBSC30. This suggests that the bolts are quite loose for 50%, while for the 30% of the tightening force the connection has no slipping resistance left. Furthermore, the differences in the periods/frequencies of oscillations are visible and in line with the expectations.

When the full response of 5 s is observed, the beating effect can be noticed. We will discuss this phenomenon thoroughly in Section 2.4.2.1. An important observation is that the first amplitude of acceleration is practically invariant to the value of the tightening force. This fact will be employed to define the load release function of the numerical model in Section 3.4.1.

Regarding the ASRs, all three models return similar fundamental eigenfrequencies and the differences correspond to the respective bolt tightening forces. Additionally, the ASRs suggest that the damping increases with the reduction of the bolt tightening force.

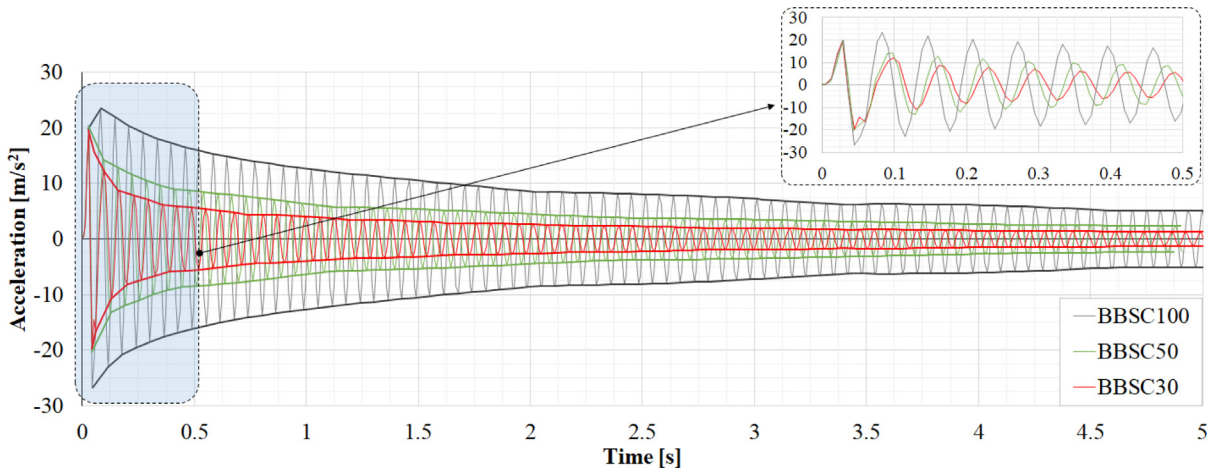

Fig. 4. Bolted beam splice connection. Experimental acceleration time histories and their envelopes for the models with three different bolt tightening forces.

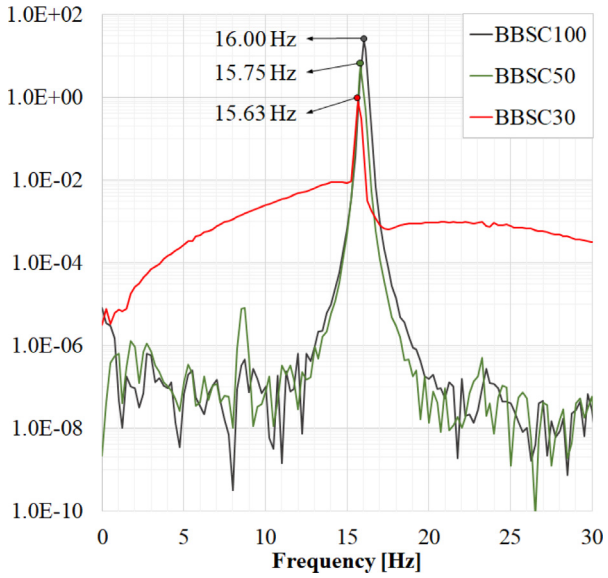

Fig. 5. Bolted beam splice connection. Auto spectrum response.

2.3.2. Model with welded beam splice connection

During the analysis of the WBSC experimental results, a lot of noise was found for the loading case with respect to the major principal axes of inertia. The ASR can be extracted, but the acceleration results are unusable for our analysis and are omitted here. Regarding the loading with respect to the minor principal axis, the acceleration response is shown in Fig. 6. Again, the beating effect is present and it will be discussed later in Section 2.4.2.1. An approximate envelope of amplitudes is plotted on the same graph using the standard exponential law for the amplitude decay of the linear single degree-of-freedom (SDOF) system. Evidently, this envelope nicely fits the acceleration amplitudes, suggesting that the WBSC oscillates in a linear range and that it can be approximated with an SDOF. This confirms our assumption from Section 2.2.1: the WBSC is practically monolithic and it can dissipate energy only via material damping. This linear response of the WBSC model allows us to estimate the damping ratio that is close to 0.0011, which is in line with the commonly found values of material damping for steel [2,3,63].

Although the adopted numerical models are discussed in Section 3, the validation of the WBSC numerical model is given here for the sake of coherence. The adopted numerical model was analyzed using the linear modal dynamic analysis and the obtained acceleration response is given in Fig. 6. The numerical and experimental results agree reasonably well, which validates the WBSC numerical model. This fact allowed us to further calibrate the numerical models and to post-process the experimental results.

The ASR responses for the loading with respect to both principal axes are shown in Fig. 7. The lowest eigenfrequency for the case of bending with respect to the major principal axis is smaller than the one with respect to the minor axis, due to their respective fixed masses of M1= 25 kg and M1= 0 kg.

2.4. Post-processing of experimental results

The need for the integration of the obtained experimental accelerations was discussed in Section 2.1, and the utilized procedure is presented here. Additionally, we discuss the beating phenomenon and consider an approach to assess experimental damping.

2.4.1. Numerical integration of experimental accelerations

Through the numerical integration of a discrete signal, we aim to find the new value v_{i+1} based on the known value v_i. This is achieved by calculating the area under a curve being integrated, between the points i and $i+1$. In this work, we have calculated the experimental velocities by approximating the discrete acceleration data with a cubic polynomial, and then integrating it with Simpson's 3/8 rule [90].

First, we have integrated the experimental acceleration response of the WBSC model. As discussed in Sections 2.2.1 and 2.3.2, this model has a linear response. This allowed us to verify the numerical integration procedure by comparing the WBSC experimental velocities with the velocities obtained using the modal dynamic procedure in Abaqus. The results agree well and are omitted for the sake of brevity. By means of this analysis, the accuracy of applied cubic numerical integration is verified. The procedure is then utilized to find the velocity time histories of the experimental BBSC models with three levels of bolt tightening force. The results are shown in the next subsection.

2.4.2. Approximate calculation of damping

As shown in Section 2.3.2, the WBSC model amplitude decay follows an exponential law, meaning that the energy dissipation of such a system can be described with one parameter: material damping. On the other hand, the BBSC model dissipates energy through a nonlinear mechanism due to the frictional slipping between the contacting surfaces. The energy dissipation and amplitude decay of such a system cannot, in general, be described with only one parameter.

There is a variety of methods that can be used to identify damping characteristics of a nonlinear system with multiple DOFs. The peak amplitude method is applied for the nonlinear response of shear lap

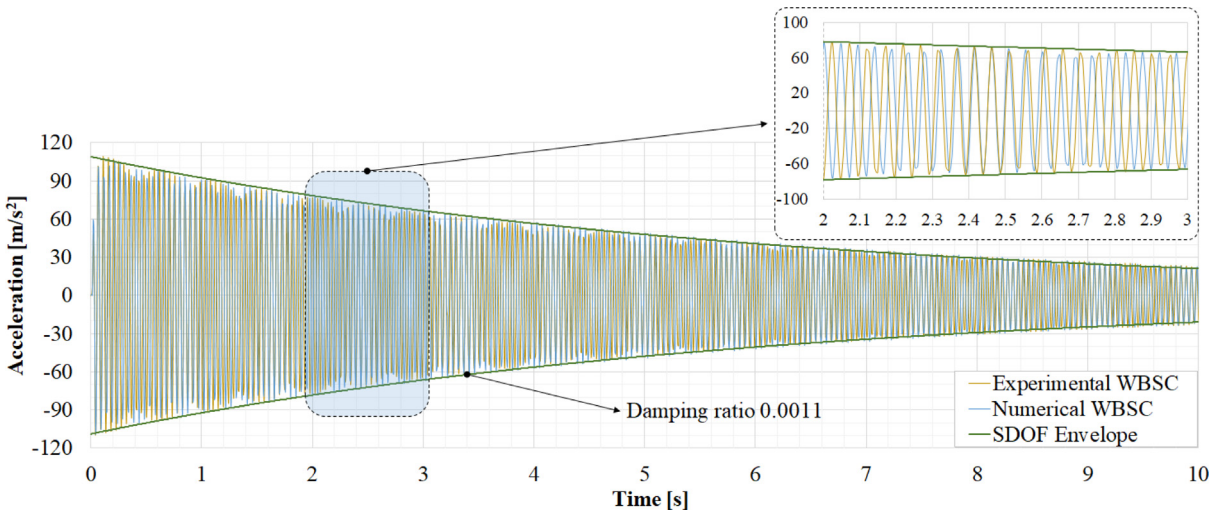

Fig. 6. Welded beam splice connection. Experimental and numerical acceleration time histories, and the envelope of a linear single-degree-of-freedom system.

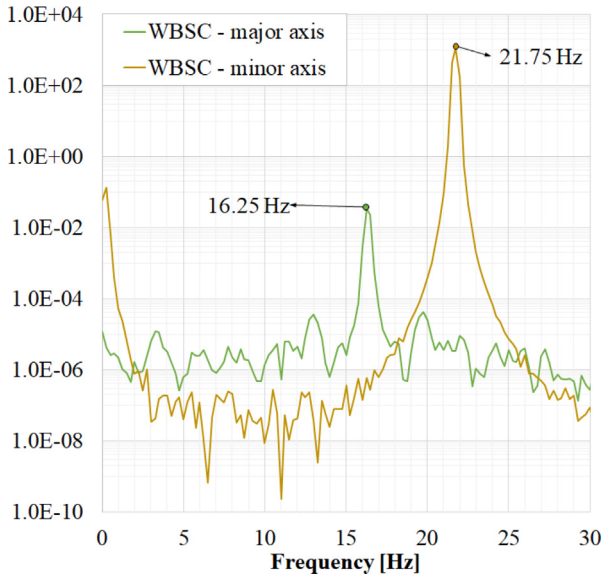

Fig. 7. Welded beam splice connection. Auto spectrum responses for two cases of loading.

joints in [62]. Damping of structures with bolted connections was considered by Goyder et al. [63,91,92]. Their algorithm is based on fitting the decaying amplitudes along short time intervals using the sine function. Here, we are using an approach similar to the one in [91].

2.4.2.1. Experimental damping of the beam with welded connection. Since the WBSC model is linear, it is well-suited to verify the algorithm for the extraction of damping. Let us assume that the decay rate between two consecutive amplitudes with the same sign is small enough to allow an approximation using the linear oscillator with viscous damping [91]. This is a reasonable assumption for small time increments between amplitudes. Therefore, we have calculated a discrete set of logarithmic decrements δ_i between all pairs of consecutive positive or negative velocity amplitudes. The damping ratio is then found by the standard expression $\xi_i = \delta_i / \sqrt{4\pi^2 + \delta_i^2}$. In this way, we have obtained a set of approximate discrete damping ratios for a complete system response.

Envelopes of the velocity and the calculated discrete damping ratios for the WBSC model are shown in Fig. 8. Due to the presence of beating, the discrete damping ratios oscillate between positive and negative values. The beating phenomenon occurs when the body oscillates in two different eigenmodes with slightly different frequencies. Manufacturing imperfections, the eccentricity of mass, and similar values of two eigenfrequencies can cause a beam to beat. The beam then oscillates with respect to both of its principal axes, and thus in more than one frequency [3]. During such vibrations, the signal appears to be modulated. This is evident in Fig. 8 where the velocity amplitudes decrease, but oscillate in regular intervals.

One typical part of the response (AC interval) is observed in the following. Between points A and B, the nonphysical negative discrete damping ratio occurs because the amplitudes increase in that time interval due to beating. Point B is the local maximum of velocity where the discrete damping ratio is zero. The amplitudes decrease in the interval BC and the damping is positive. The discrete damping ratio reaches the maximum just before point C where the beating cycle starts again.

Therefore, due to the beating effect, the discrete damping ratios do not correspond to the true values of damping. This problem is solved by fitting the damping curve through the discrete set of damping data. Since the WBSC is linear, a simple mean value data fitting is suitable and the result is displayed in Fig. 8. The realistic value of damping is obtained, $\xi = 0.00106$, which agrees with the value calculated using the decaying envelope for the SDOF system with viscous damping, $\xi = 0.0011$, cf. Section 2.3.2. This analysis shows that the beating phenomenon has a negligible influence on the damping ratio.

Due to significant noise, we have omitted the time histories of the WBSC model loaded with respect to the major axis. Nevertheless, the described damping-extraction procedure works even for such noisy experimental data. The obtained damping value is approximately 0.001. This finding suggests that the influence of geometry on the material damping is negligible for our WBSC model, cf. Section 2.2.1.

2.4.2.2. Experimental damping of the beam with bolted connection. As discussed previously, the damping ratio of the BBSC model is not constant during the free vibration response. A straightforward approach for the quasi-viscous approximation of damping is illustrated in Fig. 9, where the velocity amplitude decay for the BBSC100 model is considered. Two envelopes of the linear viscous SDOF system are utilized to estimate the damping. The first envelope approximates the energy dissipation during the short initial part of the response for $t < 0.4$ s with an approximate damping ratio of $\xi = 0.012$. The other envelope corresponds to the damping ratio of $\xi = 0.002$ and it fits the response for $t > 1.45$ s, which is linear. The middle part of the time history can be considered as a transition interval between the nonlinear and the linear response. We can improve the accuracy of this approximation by increasing the number of envelopes, and the limit case corresponds to

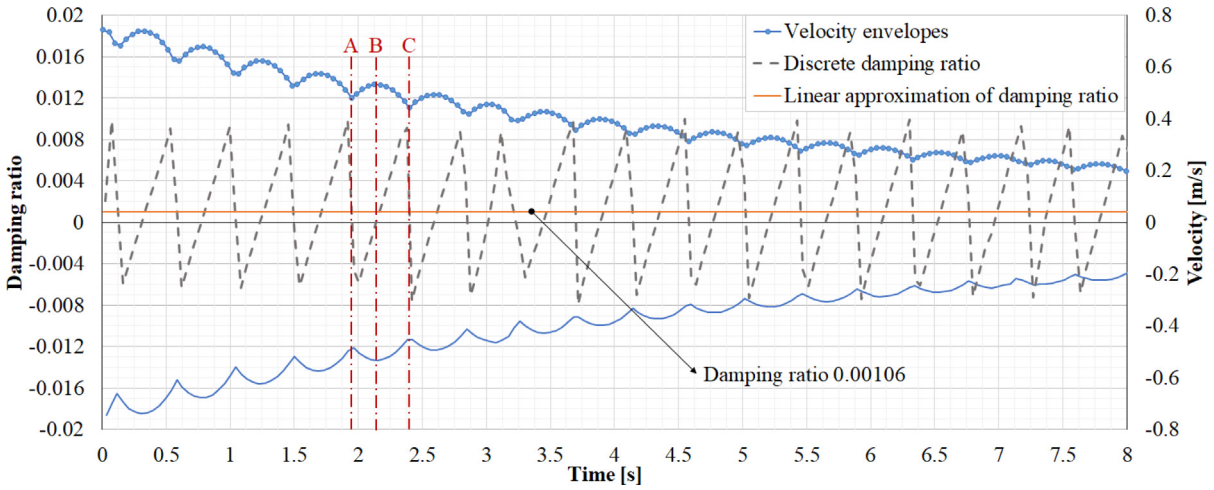

Fig. 8. Welded beam splice connection. Velocity amplitudes, discrete damping ratios and linear approximation of damping ratio.

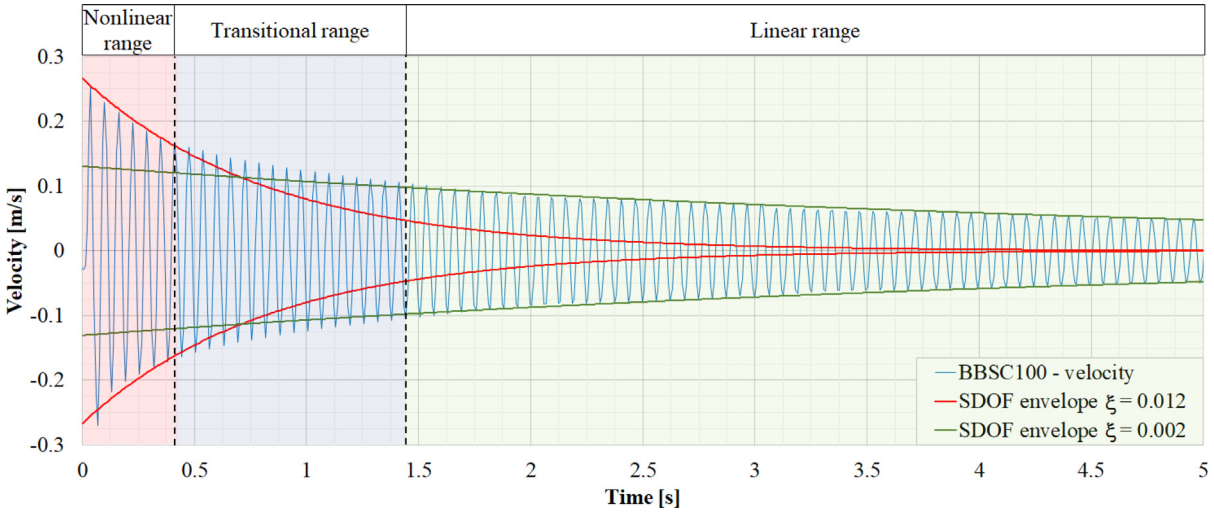

Fig. 9. Bolted beam splice connection with 100% of bolt tightening force. Approximation of damping with two decaying envelopes of the SDOF system.

the method for the calculation of the discrete damping ratios, described in Section 2.4.2.1.

To approximate the nonlinear damping characteristics of the BBSC, a function that fits the discrete damping data is required. This function is found by solving the corresponding optimization problem using the Matlab Optimization Toolbox [93]. The adopted model function consists of two decaying exponential functions, $f_m = b_1 e^{a_1 t} + b_2 e^{a_2 t}$. Coefficients a_i and b_i are found in a least-squares sense by minimizing the square error between the measured input data and the model function. The lower bound for a_i coefficients is set to zero. In this way, the adopted model function can represent both the nonlinear and constant parts of damping [62]. In order to get the global optimum, the multistart procedure is applied and the optimization problem is solved for 100 different initial starting points. More details about the theory and the application of this algorithm can be found in [94].

In this way, we found the functions that fit the discrete damping ratios, and the results are displayed in Fig. 10a, b, and c, next to the velocity envelopes discussed in Section 2.4.1. Additionally, the damping ratios for all experimental models are compared in Fig. 10d. The obtained results clearly illustrate the strong influence that the bolt tightening forces have on structural damping. Furthermore, the nonlinear change of the damping is clearly pronounced during the initial part of the time history. As time elapses, all models slowly approach the constant value of damping. Thus, after enough energy dissipates through the structural damping, the slipping in the BBSC deactivates, and the beam continues to oscillate with material damping.

3. Numerical analysis

In this section, we give key information on the adopted numerical model and its validation, calibration and verification. The basic introduction, focused on the time integration schemes, is given in the next subsection. The validation is delivered in Section 3.2, while the details of the adopted numerical model are discussed in Section 3.3. The parameters and procedures that require calibration and verification are scrutinized in Section 3.4.

3.1. Introduction

A well-known commercial FE software Abaqus is used for the numerical analysis. There are several different methods available in Abaqus for performing dynamic simulations. The linear modal dynamics is appropriate for the analysis of the WBSC model. For the nonlinear dynamic analysis of the BBSC model, two methods are available: Abaqus/Standard which uses an implicit time integration algorithm, and Abaqus/Explicit which uses an explicit one. The explicit approach was utilized here for reasons discussed below.

An implicit dynamic procedure requires an iteration process to find the equilibrium at an unknown configuration. For complex contact

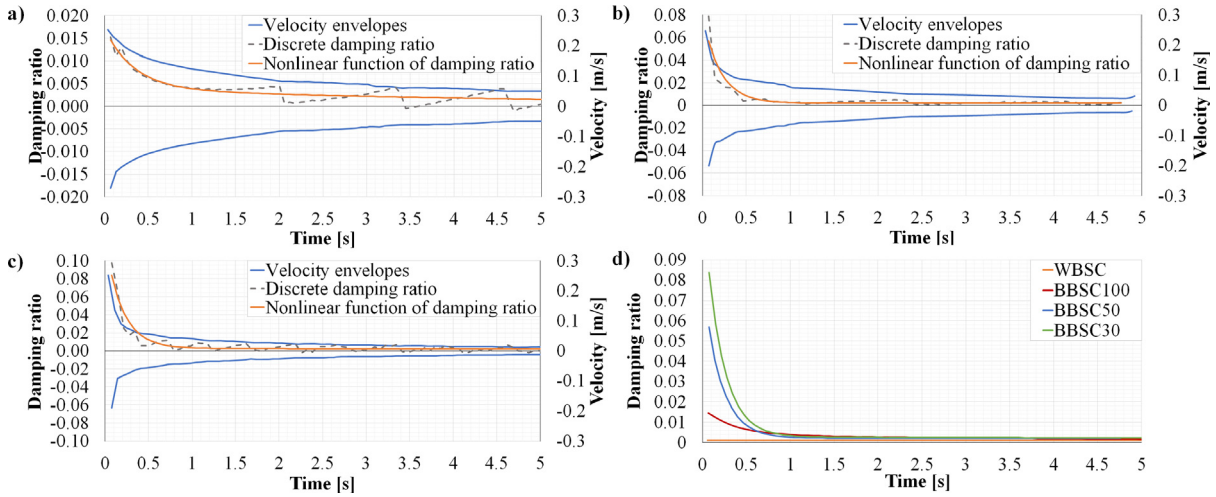

Fig. 10. Velocity amplitudes, discrete damping ratios and nonlinear function of damping ratio for: (a) BBSC100, (b) BBSC50, (c) BBSC30. (d) Comparison of damping ratios for all experimental models.

problems with many interacting parts, the implicit method is usually not recommended [8,79,80]. The main issue is the change in contact status within a time increment, which negatively affects the convergence of the nonlinear solver and yields small-time increments. For an analysis with many contact conditions, this issue makes the implicit algorithm computationally expensive. The considered BBSC model falls into this category due to the contacts between its beam parts, bolts, nuts, washers, and splice plates.

Unlike the implicit, the explicit dynamic analysis efficiently calculates large numbers of small-time increments using the central difference rule. In comparison with the implicit analysis, each increment is relatively inexpensive because the formation and inversion of the tangent stiffness matrix are not required. An important feature is that contact conditions are not of significant concern in an explicit analysis. The contact surfaces can be left in a non-contact state, rigid body movements are acceptable, and the algorithm automatically picks up the stiffness when contact is detected.

The stability limit of a time increment is the main issue of an explicit solver. The time increment typically adopted is the smallest time required for the stress wave to travel through the smallest element dimension in the model. To satisfy this condition for fine meshes and high-speed wave propagation, the time increment must be very small. When dealing with the BBSC model, it was important to find a balance between accuracy and computational time because: (i) the numerical model is relatively large with a lot of contacting surfaces that require fine meshes, (ii) the response time is 6.5 s, which is quite long for an explicit simulation. For this, we had to optimize the FE mesh and find an appropriate stable time increment.

One standard method for limiting the value of the stable time increment is *mass scaling*. When applied properly, the method can significantly improve efficiency by increasing the time increment. In order to minimize the error, mass scaling must be applied carefully to a set of elements that controls the increment size. Failure to do so can result in large artificial inertial forces that can affect significantly structural response.

The reliability of explicit nonlinear simulations is commonly assessed via energy outputs. The artificial energy should be small in comparison to internal energy, while the total energy of the overall model should be approximately constant [79].

Our numerical model is relatively complex, and it was adopted through an iterative procedure. The most important parameters that were calibrated via this process are: the FE mesh, boundary conditions, load function, contact formulation, mass scaling, reduced integration, and bulk viscosity. Furthermore, the explicit analysis does not support the bolt force option, and the bolts had to be tightened in line with the temperature change. The calibration and the adoption of these parameters are discussed further in Sections 3.3 and 3.4.

Regarding the material model, the bilinear stress–strain relationship is adopted. The beam and the splice plates have the following material properties: modulus of elasticity $E = 200$ GPa, Poisson's ratio $\nu = 0.3$, yield stress $f_y = 235$ MPa, tensile strength $f_u = 360$ MPa, and ultimate strain $\epsilon_u = 26\%$. For the bolts, nuts, and washers, the same values of E and ν are used, while $f_y = 640$ MPa, $f_u = 800$ MPa, and $\epsilon_u = 12\%$ [85].

3.2. Validation of the numerical model

Validation is an essential step which allows us to conclude if the numerical model accurately describes the experimentally-observed behavior. Here, we are presenting the results obtained with the adopted numerical model and comparing them with the experimental data. The first step of the validation is the modal analysis, while the velocity time histories are compared afterwards.

3.2.1. Modal analysis

The experimental ASR results for the BBSC and WBSC models are given in Sections 2.3.1 and 2.3.2. The adopted numerical BBSC model has eigenfrequencies of 15.61 Hz, 15.58 Hz, and 15.55 Hz for 100%, 50%, and 30% of the bolt tightening force, respectively. These values are in good correspondence with the experimental results given in Fig. 5. Actually, the differences with respect to the experimental results are less than 2.5%. It should be emphasized that the modal analysis was done in Abaqus/Standard after a static step for the tightening of bolts. However, the influence of the bolt tightening force is small because our numerical modal analysis did not capture main nonlinear effects from the deformation and slipping inside the connection.

Regarding the considered eigenfrequencies of the WBSC model, their experimental values are given in Fig. 7. The numerically obtained values are 15.7 Hz and 20.5 Hz, and they differ from the experimental ones by approximately 3% and 6% respectively, which is an acceptable alignment of results for the free vibration test.

3.2.2. Velocity time histories

The velocity time histories obtained with the adopted numerical BBSC models are compared with the experimental results in Figs. 11, 12, and 13. The experimental and numerical responses agree reasonably well, considering the complexity of the problem. The excellent correspondence of the first amplitudes is emphasized in the graphs. For example, the relative difference between the first velocity amplitudes for the BBSC100 model is around 4%. However, the agreement of

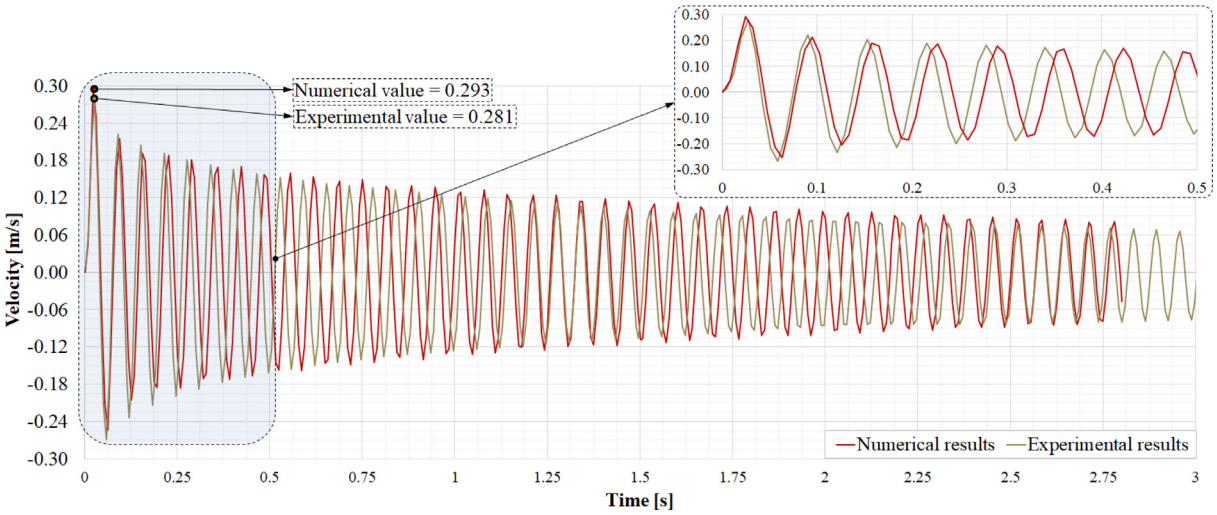

Fig. 11. Bolted beam splice connection with 100% of the bolt tightening force - BBSC100. Comparison of experimental and numerical velocity time histories.

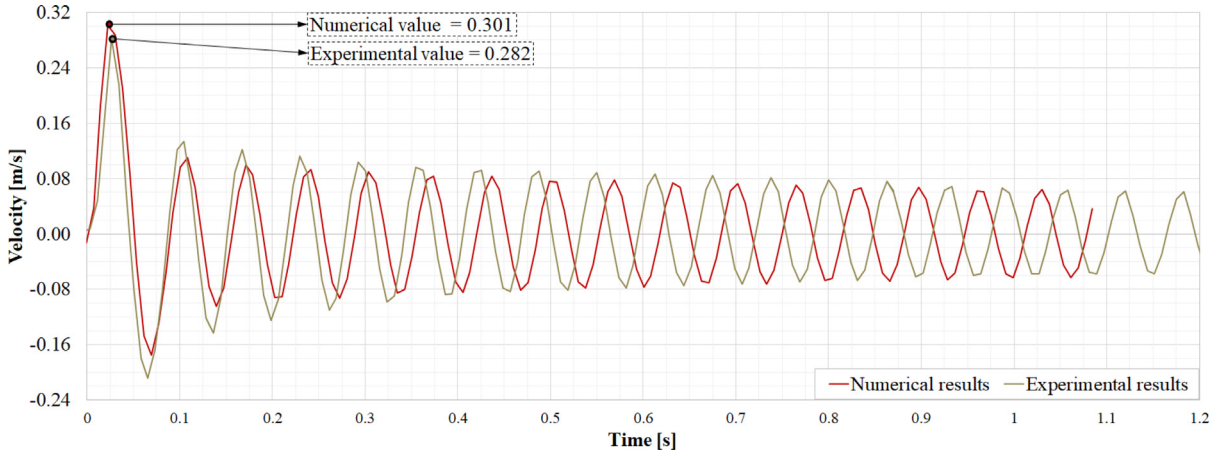

Fig. 12. Bolted beam splice connection with 50% of the bolt tightening force - BBSC50. Comparison of experimental and numerical velocity time histories.

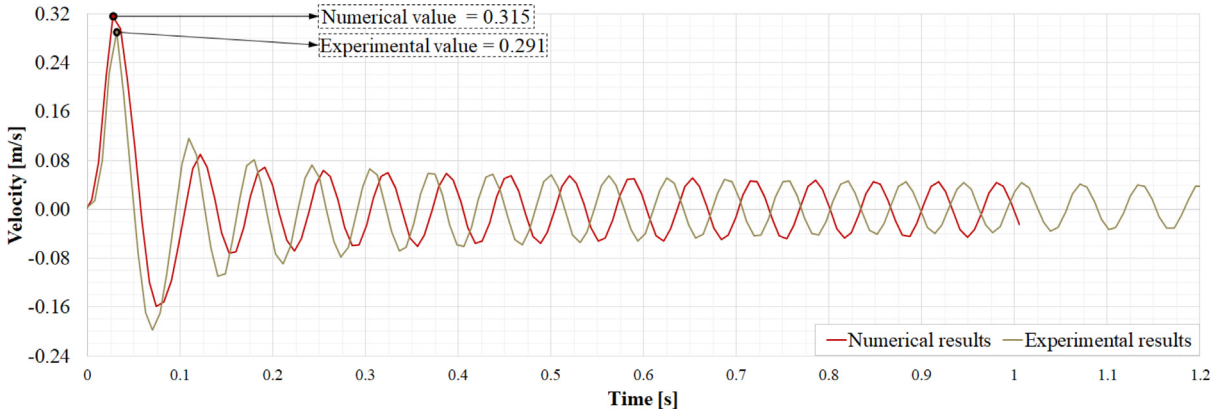

Fig. 13. Bolted beam splice connection with 30% of the bolt tightening force - BBSC30. Comparison of experimental and numerical velocity time histories.

the results deteriorates with the decrease of the bolt tightening force. Furthermore, it is evident that all experimental models oscillate with somewhat higher frequencies in comparison with the numerical models, which causes a small time shift between the compared responses. The differences between the eigenfrequencies were already discussed in the previous subsection. The differences in the velocity time histories are more pronounced due to the significant nonlinearity of the considered responses.

All in all, the observed agreement between the experimental and numerical results validates our adopted numerical model. It can simulate

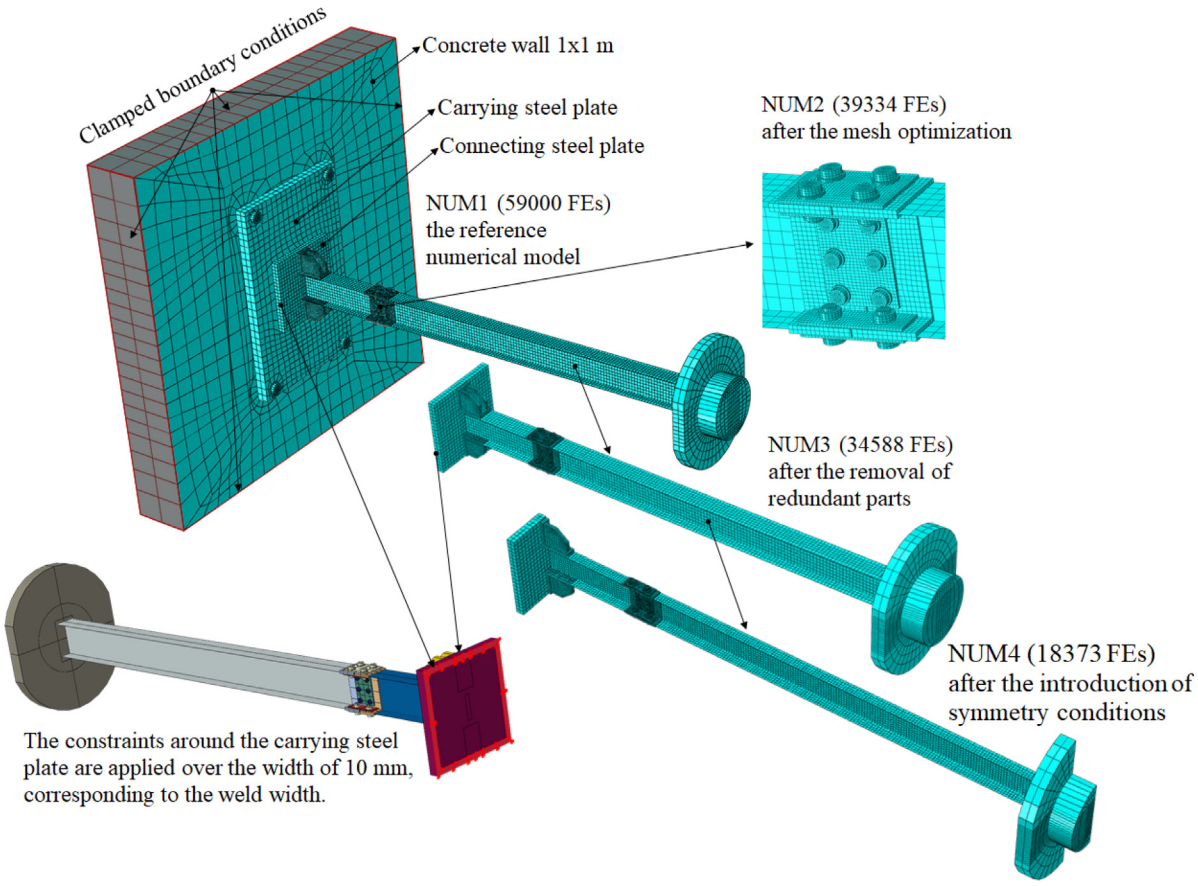

Fig. 14. Optimization of the FE mesh and the model reduction.

the realistic behavior of the observed BBSC with reasonable accuracy. This is particularly true for the BBSC100 model which is the focus of our research.

3.3. Numerical model

The main components of our adopted numerical model are discussed here: finite element mesh, contact modeling, and bolt tightening procedure.

3.3.1. Finite element mesh

To improve the balance between efficiency and accuracy, we considered the mesh optimization and model reduction. The main steps in these procedures are displayed in Fig. 14. The reference numerical model (NUM1) had all parts of the real structure: the beam is connected to the connecting and carrying plates via rigid angles, while the carrying plate is bolted to the 1×1 m section of the concrete wall that is clamped along its edges. This model is meshed with 59000 C3D8R brick elements. To optimize the mesh, the beam is remeshed with S4R shell elements, except for the connection itself, which is remeshed with C3D8R elements. As a result, model NUM2 with 39334 FEs is obtained. Next, our numerical tests suggest that the concrete wall and the carrying plate can be removed. However, this requires fixing of the connection plate along its edges and across 10 mm width, which corresponds to the weld width, see Fig. 2. The obtained NUM3 model has 34528 FEs, see Fig. 15. Connections between the shell and solid elements are modeled as shell-to-solid coupling, while the welds are modeled as tie constraints. The thickness of the welds is taken into account, and the WBSC model is also shown in Fig. 15.

Finally, by introducing the symmetry conditions and additional mesh refinement, the NUM4 model with 18373 FEs is obtained, Fig. 14. The size of the initial NUM1 mesh is reduced approximately by a factor of 3. The adopted NUM4 model is verified through a comparison of linear acceleration time histories with the NUM1 model. The agreement between the obtained results is satisfactory, and the NUM4 model is adopted for further considerations. The results are omitted for the sake of brevity.

3.3.2. Contact modeling

The contact modeling is crucial for the analysis of the BBSC model due to contact interactions between different surfaces and associated effects of the local stick/slip behavior. A considerable effort is required for the calibration of interaction properties and master/slave surfaces. A common algorithm for contact problem solving is the penalty method, which is available in both Abaqus/Explicit and Abaqus/Standard. Other approaches, such as the Lagrange multiplier method, or the Perturbed and Augmented Lagrangian methods, are available in Abaqus/Standard only [79,80].

Abaqus/Explicit offers two contact algorithms: general contact (GC) and contact pair (CP). Both of them have advantages and disadvantages that depend on the problem size, required level of detail, expected accuracy, etc. [24,25,80]. The main difference between these two contact algorithms is contact discretization. The GC method uses node-to-surface, while the CP algorithm employs surface-to-surface discretization. GC is a robust, accurate, and efficient algorithm that allows straightforward modeling of contact interactions between multiple bodies. The node-to-surface discretization is a method where each contact constraint involves a slave node and a master face. One issue of this approach is the penetration of slave surfaces by master nodes, which affects the solution. A mesh refinement of slave surfaces is a simple way to tackle this issue.

On the other hand, the CP algorithm is not as simple to use as GC. It requires an explicit definition of all interacting surface pairs, along with the properties, constraints, and master/slave surfaces for each contact

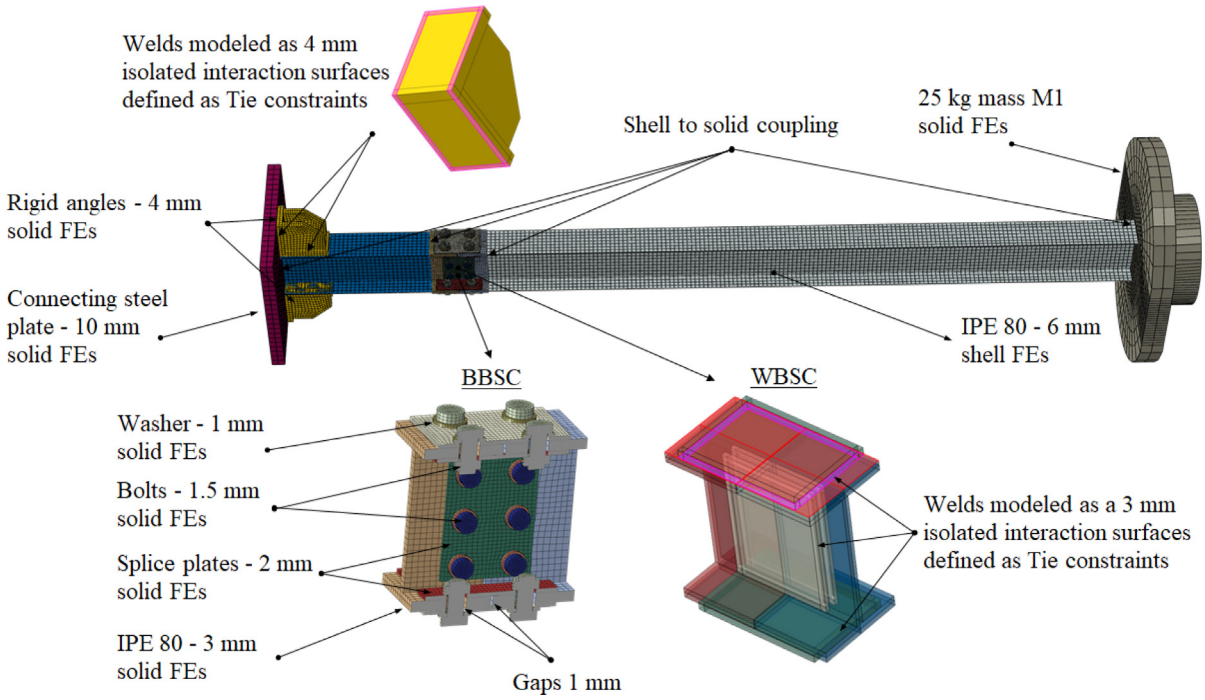

Fig. 15. NUM3 model. Types of elements and their approximate dimensions. Application of shell to solid coupling and tie constrains between parts of the model.

pair. The surface-to-surface formulation detects contact conditions in regions around the slave nodes, rather than only at the individual slave nodes. These regions are approximately centered around slave nodes, so each contact constraint predominantly utilizes one node, but also considers the adjacent ones. The surface-to-surface algorithms do not suffer from the penetration issues between nodes and master/slave contacting surfaces. Unlike the node-to-surface, the surface-to-surface algorithms are not sensitive to the master/slave roles between contacting surfaces. Furthermore, they can reduce local penetrations and improve the accuracy of contact stresses even for non-matching meshes. However, it is recommended that the slave surface has denser mesh than the master surface, while the stiffer body should be assigned as a master.

Both the GC and CP algorithms were utilized here for the analysis of the BBSC model in order to investigate their pros and cons. Contact interaction was defined between all components of the BBSC: the beam parts, bolts, washers, and splice plates. To simplify the GC numerical model, we have defined the individual surface pairs that are expected to interact. Since GC supports the definition of multiple interacting surfaces between different parts, the BBSC was modeled with 24 individual contact pairs. Regarding the CP approach, each contact interaction pair needs to be defined. Also, contact interaction can consist of only one surface from each of the two parts. These requirements resulted in 69 contact surface pairs for the CP model. The balanced master/slave weighting is applied for both GC and CP, and the weighting factor is set to $f = 0.5$ for the CP case.

Let us emphasize that we used GC for the major part of our research, due to its simplicity. Therefore, all the presented results, until Section 3.4.4, are given for the GC contact algorithm.

Contact interaction along the normal direction is defined as normal hard contact, allowing the separation between the interacting surfaces. The penalty friction method with finite sliding, based on Coulomb's law of friction, is utilized for the tangential contact behavior. The isotropic Coulomb's law of friction assumes that there is no relative tangential motion when the frictional shear stress is less than some critical stress that is proportional to contact pressure. Even for models without relative sliding, the numerical implementation of the Coulomb friction through the penalty method allows some elastic slipping in

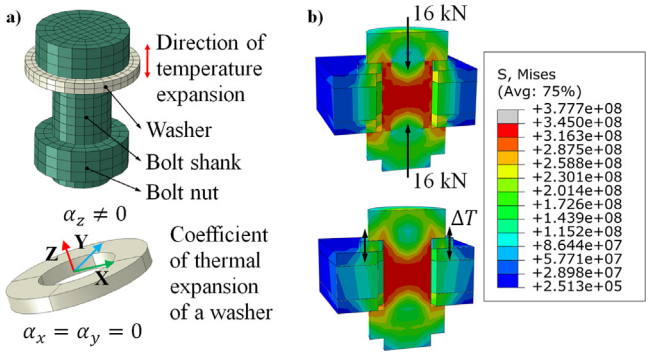

Fig. 16. Tightening of bolts. (a) Model of a bolt, nut, and washer. The thermal expansion coefficients for the washer. (b) Distribution of the von Mises stresses for the bolt force and temperature change methods.

contact interaction due to the finite stiffness of penalty springs. As mentioned in Section 1, the coefficient of friction has a crucial role in the analysis of mechanical connections and it can strongly affect nonlinear structural response. For the friction between steel surfaces, the friction coefficient varies from 0.1 to 0.8 [15–17,24,39–41,85]. This broad range of values is caused by a variety of parameters that influence friction, as discussed in Section 1. We have conducted detailed numerical analyses to find the most suitable friction coefficient for the problem at hand, and the value of $\mu = 0.155$ was adopted. A similar value for the friction between steel parts can be found in works that investigate bolted connections [15,39,95–97].

3.3.3. Tightening of bolts

A standard bolt connection consists of a bolt, nut, and washer. To limit the number of contact surfaces, the bolt and nut are here modeled as a single body, Fig. 16a. Abaqus supports two methods for the bolt tightening: applying a bolt force and adjusting the length of the bolt shank. However, neither of these options are supported by Abaqus/Explicit.

There are several alternative approaches in the literature for the tightening of bolts in Abaqus/Explicit. One method is based on detailed modeling of threads on the shank and inside the nut, and it is called *turn-of-nut* [98]. The bolt pretension is then introduced by rotating the nut. Another approach is to apply a temperature change to either the bolt shank [8] or to the washer [99,100]. The latter approach was employed in our numerical model by applying a temperature change to the washer.

The washer was made from an orthotropic material with a non-zero thermal expansion coefficient along the bolt direction, Fig. 16a. Prior to the application of mass M2, the washer was subjected to the positive temperature change, causing volume expansion along the z direction and producing tension in the bolt shank. With proper calibration of the temperature load, the required tightening force was obtained. For verification purposes, a numerical model that utilizes static bolt force was made in Abaqus/Standard. The von Mises stress distributions in the bolt at the final step of loading are displayed in Fig. 16b. The stresses are practically the same for both the temperature method and the bolt force procedure.

3.4. Calibration and verification of the numerical model

The calibration and verification are closely related to the validation. The numerical model has to be adopted through a series of iterations until the results are consistent and aligned with the experiment. The adopted numerical model is validated in Section 3.2, while the calibration and verification of the main parameters are discussed in this subsection. Some of the intermediate numerical results are compared with the experimental results to emphasize the iterative nature of the calibration process and its relation to the validation. First, we are calibrating the load function that is separated into two parts: load application and load release functions. This is followed by a discussion and verification of proper mass scaling. Then, the influences of bulk viscosity, order of numerical integration, and contact formulation on structural response are considered. Finally, the quality of the numerical solution is assessed through the analysis of the model's energies.

3.4.1. Load release function

Let us consider the load release function that describes the removal of additional mass M2. Since the load release time Δt_{LR} is relatively short, the linear function is adopted. The experimental results in Fig. 4 suggest that the bolt tightening force does not significantly affect the first amplitude of acceleration. Due to this fact, the load release time was calibrated with respect to the first acceleration amplitude. Five different load release time intervals are tested via the modal dynamic analysis using $\xi = 0.012$, see Fig. 9. The envelopes of numerically-obtained accelerations and the experimental acceleration time history are shown in Fig. 17a. The obtained envelopes reveal that the first amplitude converges with respect to the load release time. Therefore, the value $\Delta t_{LR} = 0.015$ s was adopted in our numerical model.

The first 0.4 s of the acceleration and velocity time histories are calculated with the modal analysis and compared with the experimental results in Fig. 17b and c. By using the adopted load release time $\Delta t_{LR} = 0.015$ s, the numerical and experimental results agree reasonably well. Additionally, the adopted load release time is validated by comparing the first velocity amplitudes in Section 3.2.2.

3.4.2. Load application function

The load application function is adopted by balancing efficiency and accuracy. It must be short enough to allow reasonable calculation time, but long enough to simulate static loading that does not affect the free vibration response. After several tests, the circular function and the load application time $\Delta t_{LA} = 3.5$ s are adopted, see Fig. 18. The load function is defined in the time interval $t \in [-3.515, 0]$, while the pretension of bolts takes place for $t \in [-3.715, -3.515]$. After the load release, the free vibration response occurs during the interval $t \in [0, 2.8]$. The displacement time history in Fig. 18 clearly indicates a significant sudden movement after approximately 0.5 s of the load application. This large displacement is caused by the macro slip in the bolted connection; the dependent part of the beam suddenly rotates with respect to the clamped part and the splice plates bend. This initial macro slip was also designed and observed in the experiment, see the illustrations of numerical and experimental BBSCs in Fig. 18 and discussion in Section 2.2.3. As a result, a complex stress state arises in the connection and it is further discussed in Section 3.4.4. After the initial macro slip and the load release, the beam oscillates with respect to a newly-found static equilibrium position.

In order to scrutinize the influence of load application time, the velocity time histories for three values of Δt_{LA} are shown in Fig. 19. Regardless of the load application time, the macro slip occurs. The main difference between obtained responses is that, for $\Delta t_{LA} = 5.5$ s, the velocity amplitudes damp almost completely before the load release, in contrast to the other two models. The full damping of the structure before the load release would be an ideal case, but also non-efficient due to the long load application time. The obtained results suggest that the velocity responses of models with $\Delta t_{LA} = 3.5$ s and $\Delta t_{LA} = 5.5$ s, for $t > 0$, are practically indistinguishable, while the model with $\Delta t_{LA} = 2.5$ s gives similar amplitudes but is slightly shifted in time. These observations provide an argument to adopt the value $\Delta t_{LA} = 3.5$ s.

Regarding the displacement time histories, it is evident that the model with the slowest application of load, $\Delta t_{LA} = 5.5$ s, has the smallest displacement. Also, the slipping of this model occurs in two instances, and its value is lower than that of the other two models. If we focus on the instances when the slipping occurs, it is evident that the velocity peak increases with the decrease in the Δt_{LA}. This can cause significant disturbance of the free vibration response, especially if the load application time drops below 1.5 s.

3.4.3. Mass scaling

As already discussed, the crucial parameter of explicit time integration is the stable time increment. Its correct value is vital for the accuracy of numerical results, and it strongly affects computational time. This increment is equal to the time required for a wave to propagate through the smallest element dimension, and we can increase it by deliberately increasing the mass density of critical FEs. The application of mass scaling requires special attention in dynamic analysis because it introduces fictitious inertial forces. The task is to carefully select FEs for mass scaling by balancing the computational time and accuracy.

For the adopted numerical model, the selected FEs are shown in Fig. 20. These are the smallest FEs in the model and they belong to the splice plates, bolts, washers, and parts of the beam around the bolt holes. To investigate the influence that mass scaling has on the structural response, three values of the stable time increment have been tested: $\Delta t = 9.83 \times 10^{-8}$ s, $\Delta t = 2.00 \times 10^{-7}$ s, and $\Delta t = 3.40 \times 10^{-7}$ s. The reference model is the one without mass scaling, with the time increment $\Delta t = 9.83 \times 10^{-8}$ s.

The velocity time histories for these three values of Δt are shown in Fig. 21. These results imply that the model with the stable time increment of $\Delta t = 2.00 \times 10^{-7}$ s returns the same results as the reference model without mass scaling. On the contrary, the model with $\Delta t = 3.40 \times 10^{-7}$ s gives significantly different results. Following these observations, the mass scaling that returns the stable time increment of 2.00×10^{-7} has been adopted in our numerical model. As a result, the initial stable time increment has been increased by a factor of 2.03 without significantly influencing the structural response.

Additionally, the mass increase for the whole model and selected elements is depicted in Fig. 21. The mass increase of the adopted model is 1.73% for the complete structure and 145% for the selected elements. Although the mass increase of selected elements is substantial, the mass increase of the whole model is negligible and the influence of fictitious inertial forces is insignificant. For the model with $\Delta t = 3.40 \times 10^{-7}$ s, the whole mass increases by a factor of 3.3, while the mass of selected

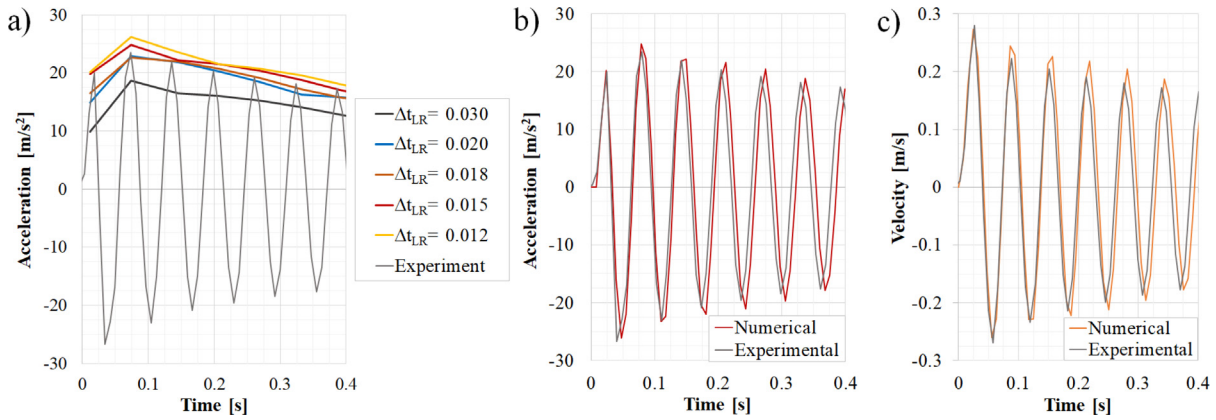

Fig. 17. Calibration of the load release time with respect to the first experimental amplitude. (a) Envelopes of acceleration for different values of the load release time Δt_{LR}. (b) Acceleration time history with $\Delta t_{LR} = 0.015$. (c) Velocity time history with $\Delta t_{LR} = 0.015$.

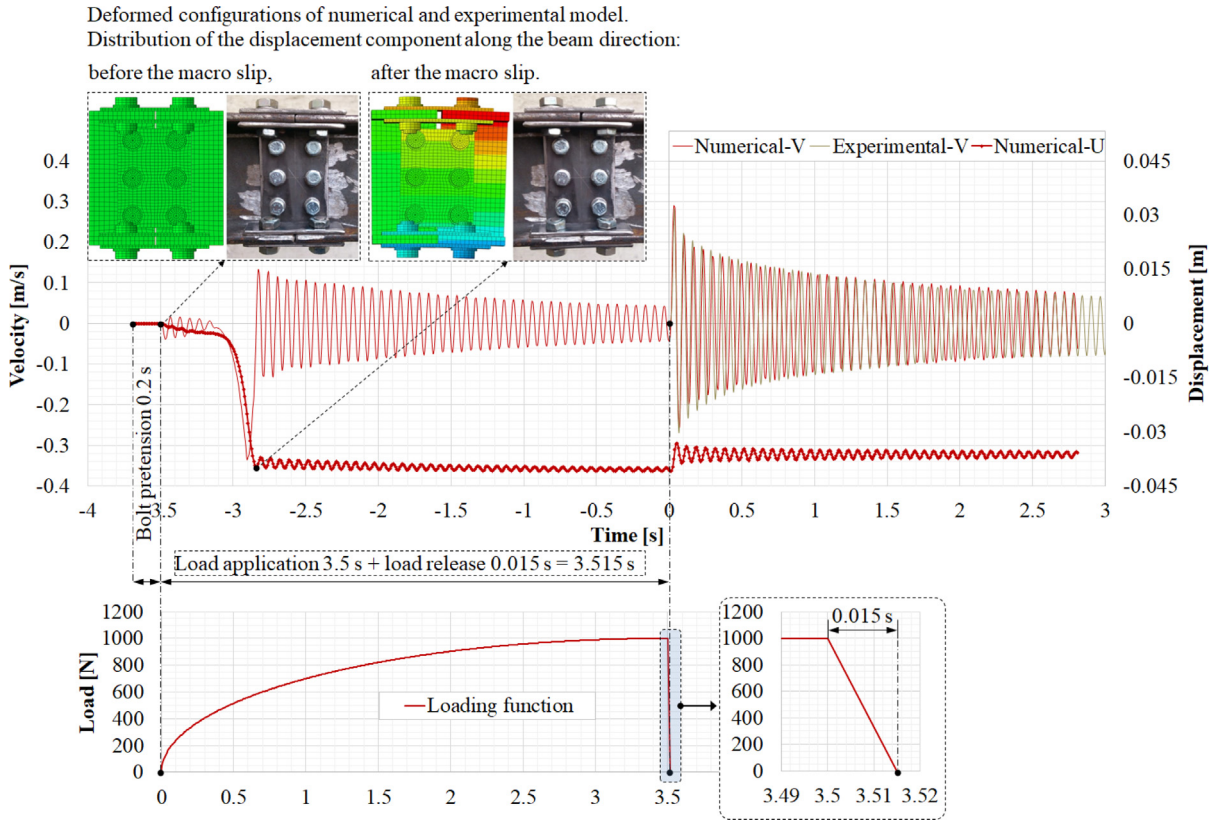

Fig. 18. Adopted load function. The velocity and displacement time histories for the adopted load function. The physical and numerical model of the BBSC before and after the macro slip.

elements rises by a factor of 160. This large increase of mass causes evident errors in the numerical response.

The reference numerical model, without mass scaling, requires 110 h of computational time for 6.5 s of simulation. By applying the adopted mass scaling, the computational time reduces to approximately 53 h, which is a valuable improvement. Let us note in passing that computational time depends on several other parameters besides mass scaling, with the order of numerical integration being the most important. In comparison with the reduced spatial integration, the full integration increases computational time of our model, on average, by more than 200%.

3.4.4. Bulk viscosity and order of integration

There are two sources of energy dissipation in our BBSC numerical model: nonlinear damping due to the friction in the bolted connection and numerical damping. Let us focus on numerical damping. The two main sources of numerical damping in Abaqus/Explicit are bulk viscosity and the order of integration. Bulk viscosity represents artificial damping proportional to volumetric straining. The addition of such a viscous pressure term to the equation of motion helps to solve high-speed dynamic events. The method is also known as the von Neuman–Richtmeyer viscosity [101,102]. Bulk viscosity in Abaqus/Explicit consists of linear and quadratic terms, and the default values were used for our numerical model.

Linear fully-integrated C3D8 elements were initially used for the splice plates, parts of the beam, washers, etc. Such a modeling approach causes issues with bending deformations. Concretely, a strong shear locking effect occurs, which artificially increases the stiffness of the structure. This issue is alleviated by implementing the C3D8R elements

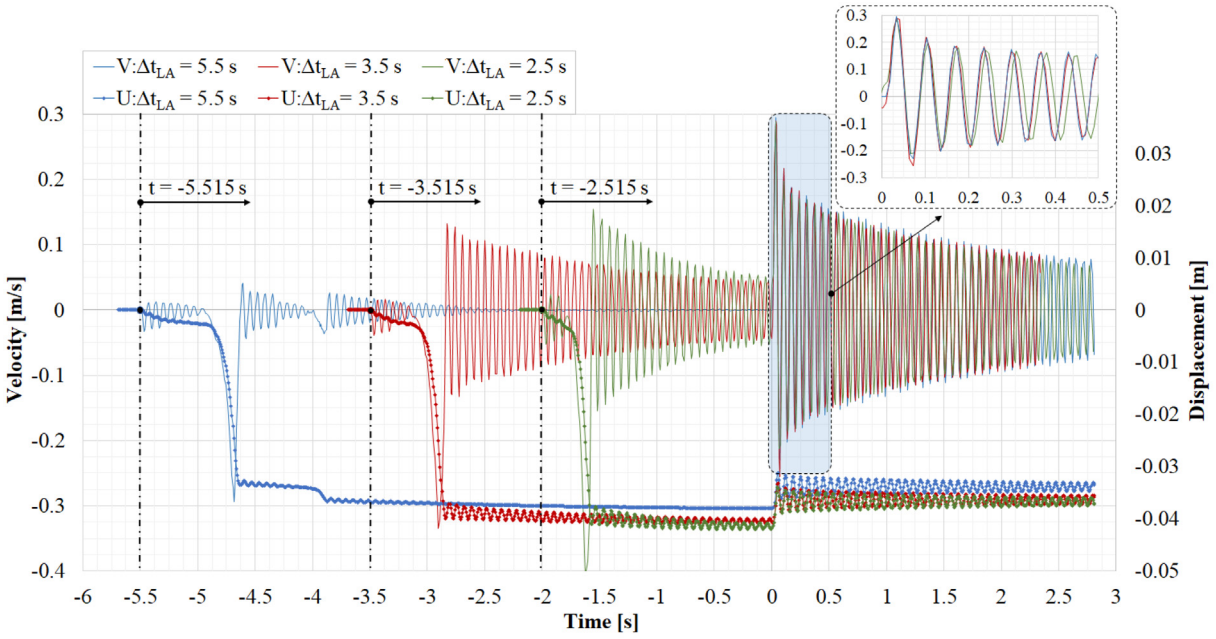

Fig. 19. Calibration of the load application time for BBSC100. Velocity and displacement time histories for: $\Delta t_{LA} = 2.5$ s, $\Delta t_{LA} = 3.5$ s, $\Delta t_{LA} = 5.5$ s.

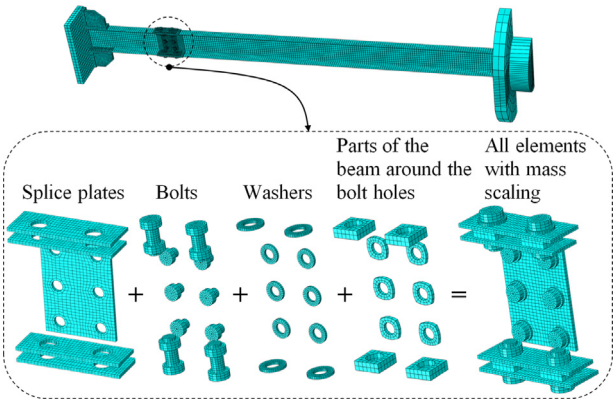

Fig. 20. Selected set of finite elements for the application of mass scaling.

with reduced integration. However, an unwanted side effect of the reduced integration is hourglassing, the distortion of elements that occurs during the bending. This phenomenon affects accuracy when the mesh across the thickness dimension is sparse [79,103,104].

Bearing this in mind, we have analyzed the numerical damping that exists in our explicit simulations. In order to exclude structural damping, the WBSC model has been considered. The adopted numerical model utilizes both the bulk viscosity and C3D8R elements. The obtained results are omitted for the sake of brevity and the resulting numerical damping is close to 0.001. This value is in excellent agreement with the material damping discussed in Section 2.3.2. Therefore, the numerical damping of the adopted numerical model corresponds to the estimated material damping of the real structure. Due to this fact, there is no need to explicitly define damping in our numerical model. Moreover, these values of the material and numerical damping are not crucial for the observed response, which is dominated by the structural damping due to friction, see Fig. 10. The main source of numerical damping in our case is reduced integration, and its effect can be alleviated by increasing the mesh density along the thickness direction.

Let us consider the influences that bulk viscosity and the order of integration have on the BBSC100 model response. Both the GC and CP contact formulations are utilized, and the velocity time histories are given in Figs. 22 and 23. Furthermore, the distributions of Mises stress in the flange splice plate at the upper part of the section, before the load release, are shown. Different models are marked as RxBx, where x takes the value of 0 or 1, while R and B represent abbreviations for **R**educed integration and **B**ulk viscosity, respectively. x = 1 indicates that a parameter is included, while x = 0 designates that a parameter is excluded.

All the results presented until this point are obtained with the GC R1B1 model. The most important observation that follows from the results in Figs. 22 and 23 is that R1B1 models are invariant with respect to the contact formulation. For the C3D8R elements, bulk viscosity does not influence velocities but it does affect stress distributions, especially when the GC formulation is employed.

Regarding the fully integrated C3D8 elements, they return erroneous results. The dominant eigenfrequency of C3D8 models is invariant with respect to the contact formulation and bulk viscosity, and its value is a bit higher than that of C3D8R models. This effect is probably caused by shear locking. Regarding the velocity amplitudes, they are higher for C3D8 elements, with the exception of the GC-R0B0 model. The full integration strongly affects stress state and results with the plastification of the splice plate. Finally, stress distributions obtained with the CP formulation are much smoother than those from the GC approach. In general, results from the CP formulation are more reliable and independent from other parameters. This is mostly due to the issues inherent in the GC point-to-surface modeling, such as penetration and snugging of master nodes.

3.4.5. Energy considerations

The energies of a numerical model are important parameters that can quantify the quality of the numerical solution. For this, four energies are observed: total energy E_{TOT}, internal energy E_I, artificial strain energy E_A, and work done by contact penalties E_{PW}. Some general guidelines are that E_{TOT} should be constant, while the ratio of E_A and E_I should be less than approximately 2–10%, depending on the model [79,105,106].

Both contact formulations are considered, and the energy time histories are shown in Figs. 24 and 25. Let us first discuss the total energy. For both contact formulations, E_{TOT} increases by a similar value during the bolt tightening in the time interval AB. This occurs because the

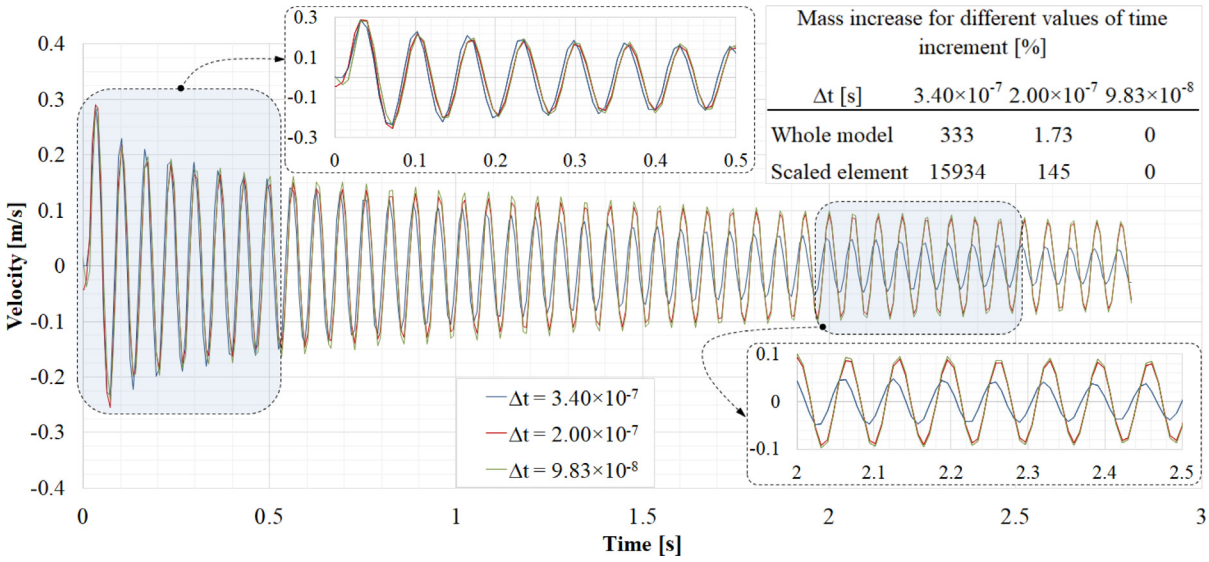

Fig. 21. Verification of mass scaling on BBSC100. Velocity time histories and mass increases for three models with different values of stable time increment Δt.

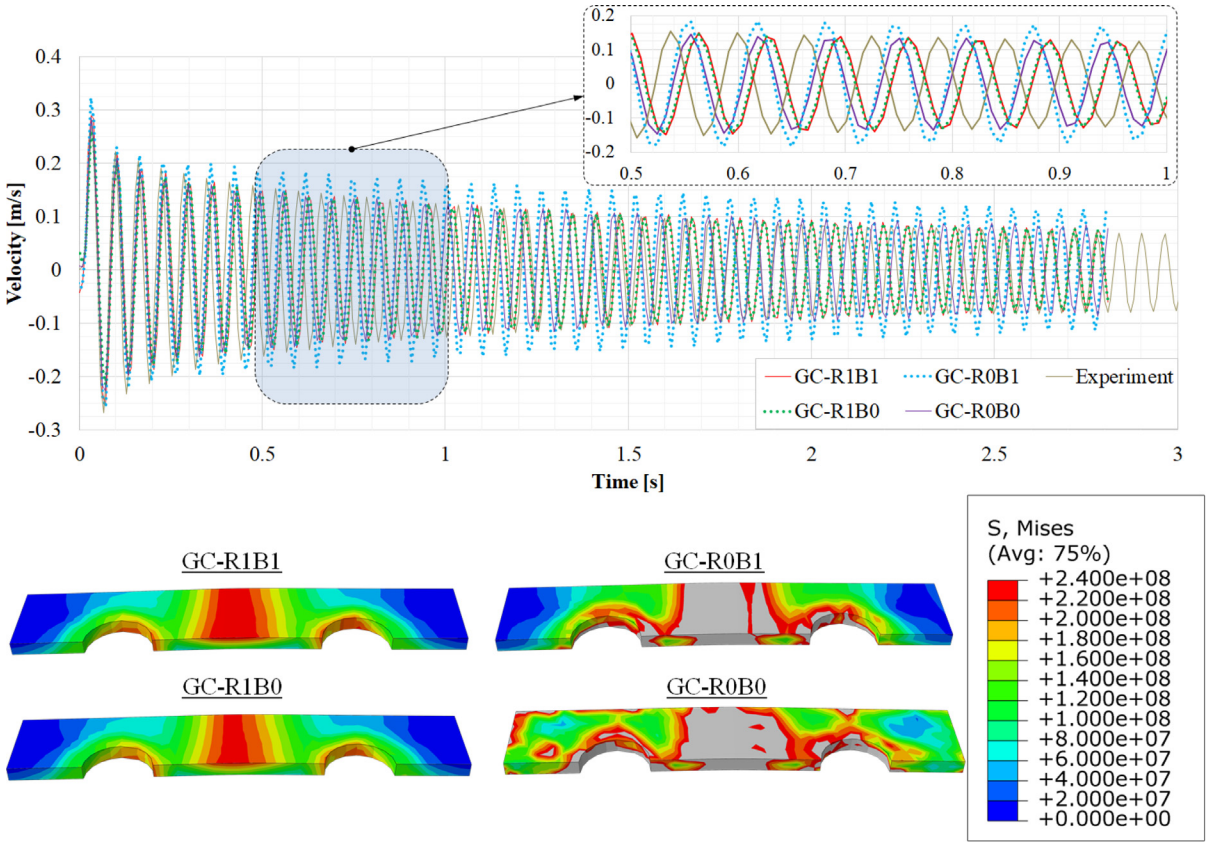

Fig. 22. Influence of bulk viscosity (B) and the order of integration (R) using the General contact (GC) formulation. Velocity time histories. Stress distributions in the flange splice plate at the upper part of the section, before the load release.

internal energy increases as a result of the temperature expansion of the washer, but there is no external work. Afterward, the total energy is constant for the GC formulation in the interval BF. However, for the CP formulation, the situation is different. Due to the significant work done by penalties, E_{PW} significantly increases in the interval CD, where the macro slipping occurs. The penalty energy is practically constant in the remaining interval DF, with the exception of small increase at the point of the load release. This increase in E_{PW} is followed by a decrease in E_{TOT}. If we consider E_{TOT} without E_{PW}, the resulting energy is practically constant. This inconsistency is specific to the adopted model with the CP formulation. This problem of non-constant total energy is often present in contact and impact problems [107,108]. If there is a significant change in E_{TOT}, it is important to double-check the results. In our case, the free vibration velocity time history in the time interval EF is not affected by this phenomenon.

Regarding the ratio between the artificial and internal energy, E_A/E_I, it is 8.5% for the CP, and 35% for the GC formulation. As such, this ratio is within the acceptable limits for the CP, and outside of the

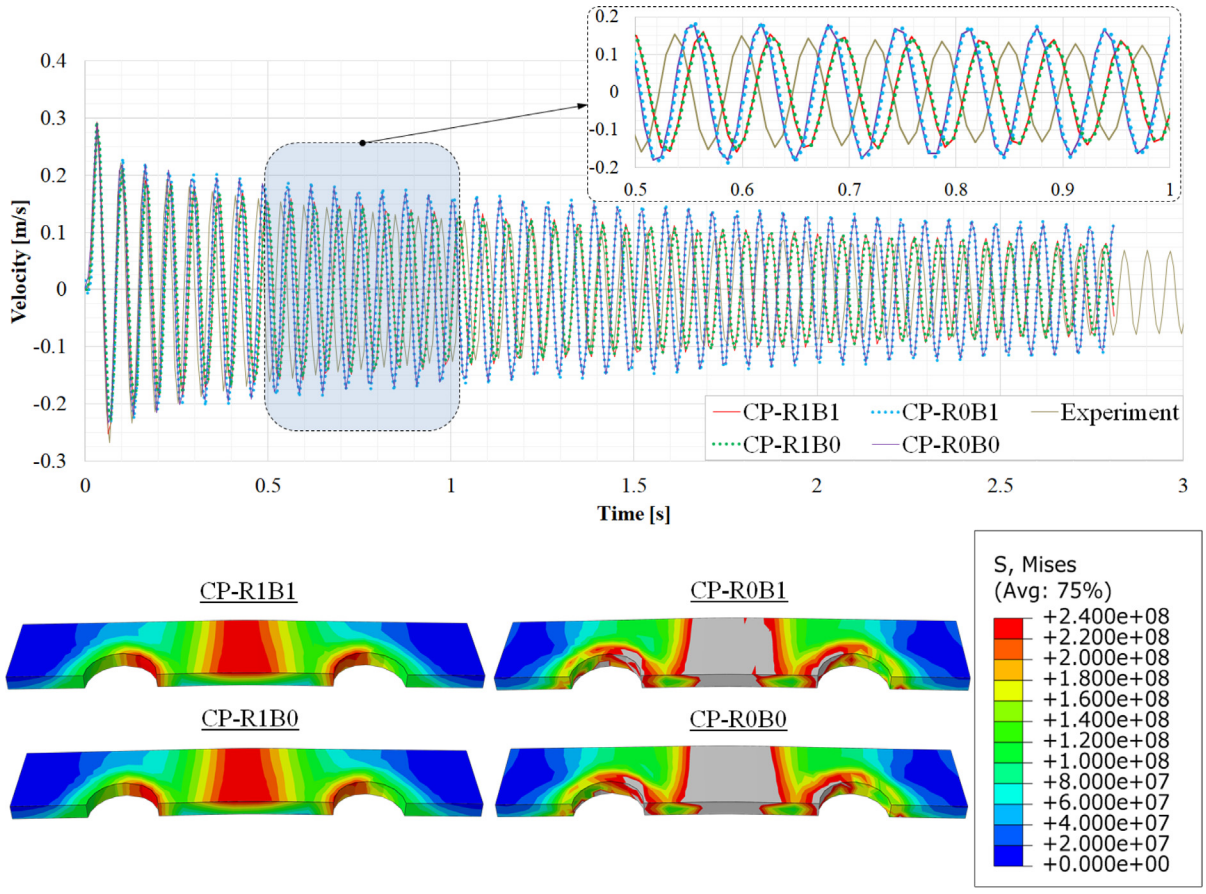

Fig. 23. Influence of bulk viscosity (B) and the order of integration (R) using the Contact pair (CP) formulation. Velocity time histories. Stress distributions in the flange splice plate at the upper part of the section, before the load release.

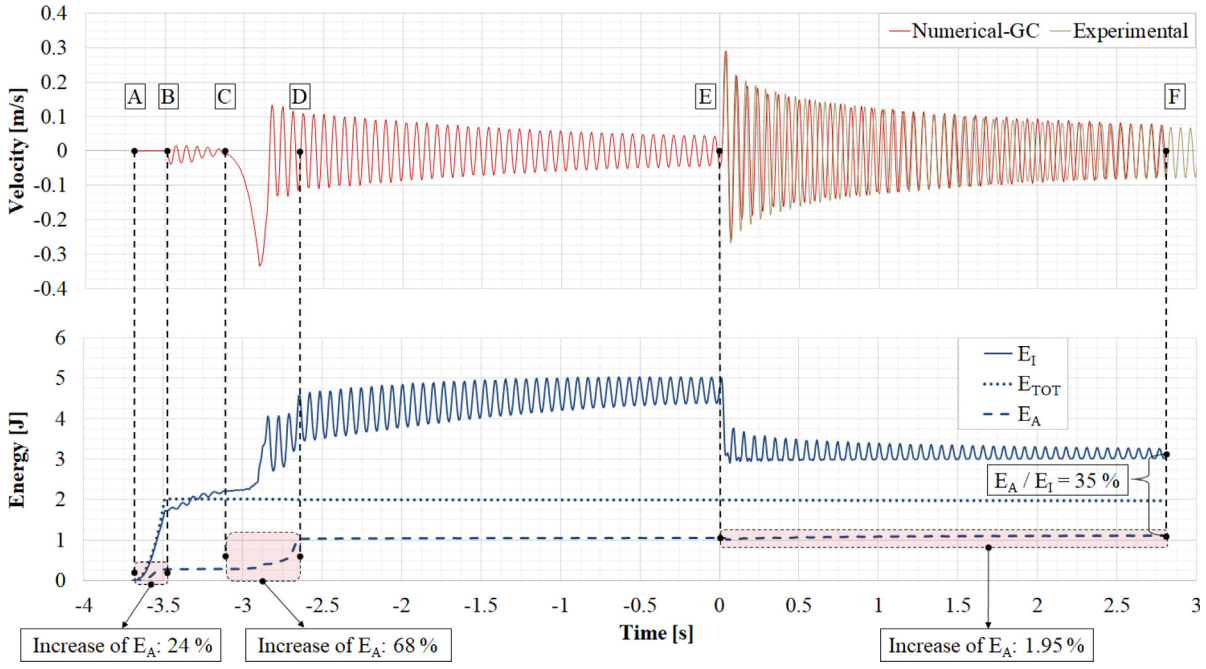

Fig. 24. Energy time histories of the GC model. Experimental and numerical velocity time histories.

limits for the GC formulation. This observation proves that surface-to-surface contact discretization helps reduce the hourglassing effect. The increase of the artificial energy predominantly occurs during the bolt tightening (time interval AB) and the macro-slipping (time interval CD). The relative increases of E_A that occur during these two intervals are similar for both contact formulations, but the absolute values are higher

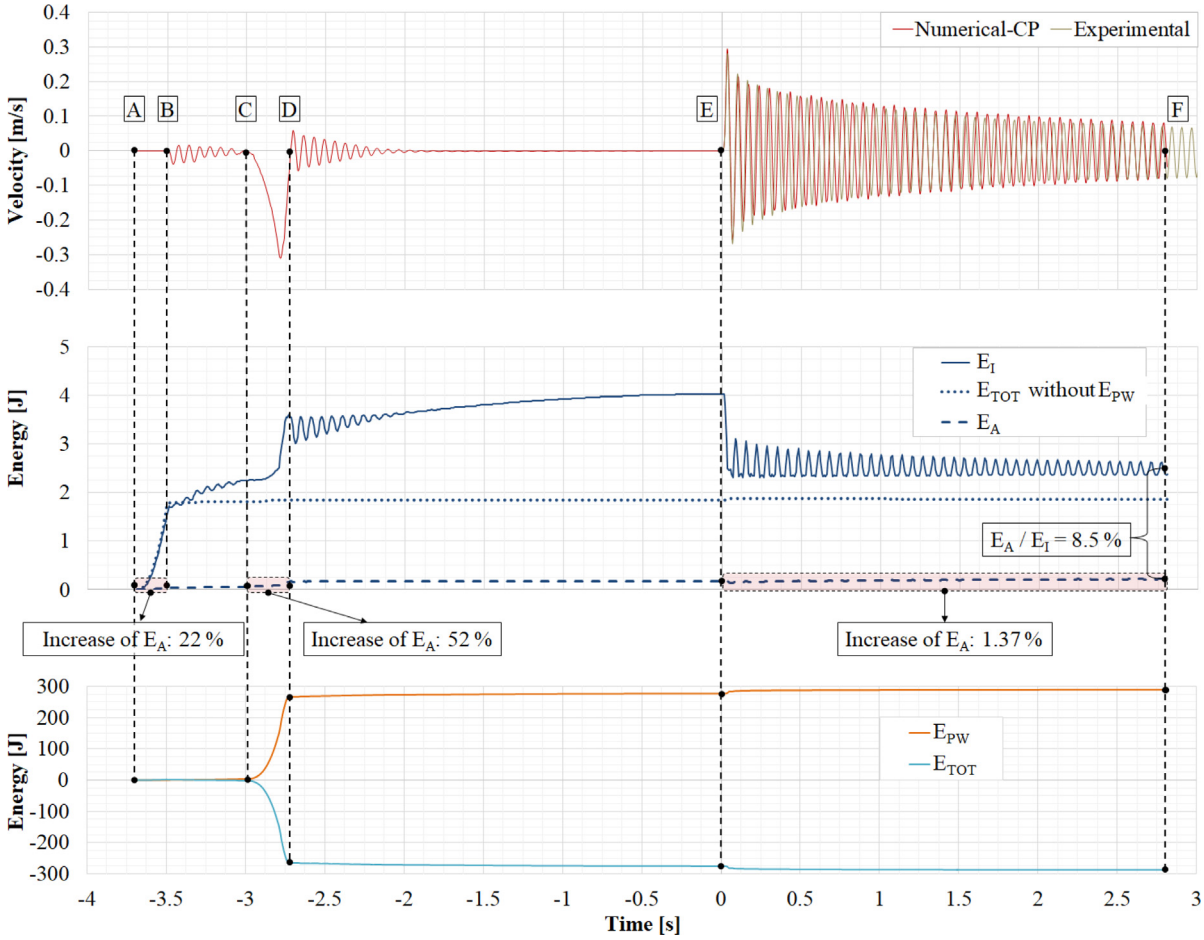

Fig. 25. Energy time histories of the CP model. Experimental and numerical velocity time histories.

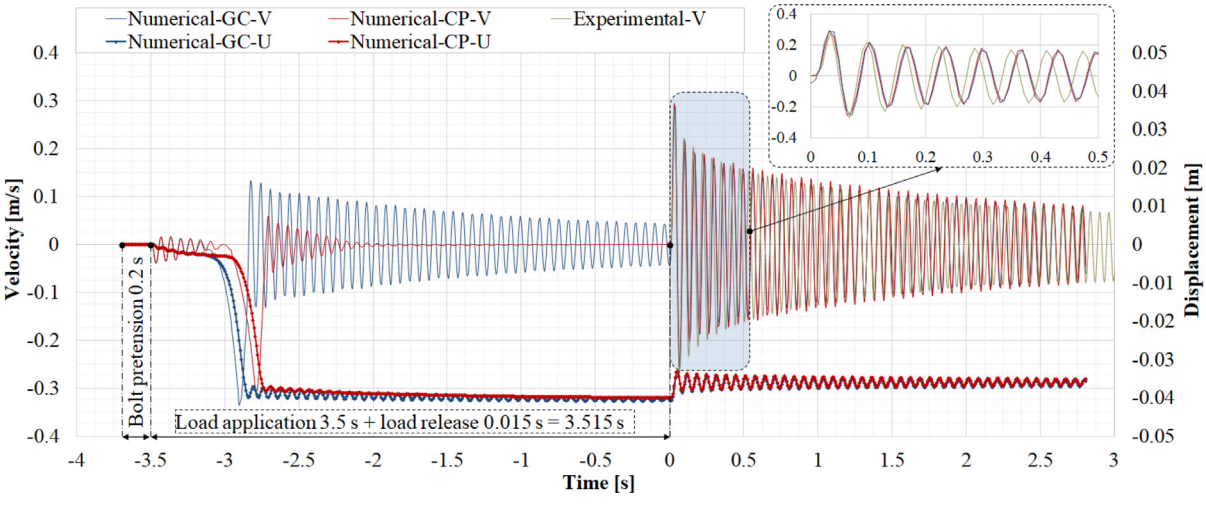

Fig. 26. Comparison of experimental and numerical time histories for both contact formulations.

for the GC formulation by a factor of 5. Since the internal energies are similar in both contact formulations, this directly affects the observed ratios E_A/E_I. The most significant fact is that the relative increase in the artificial energy is negligible during the free vibration response (time interval EF).

To scrutinize these observations, the velocity and displacement time histories for the adopted numerical model and both contact formulations are compared in Fig. 26. First, the free vibration response is not affected by the discussed energy inconsistencies in either contact formulations. The CP formulation fully dampens the vibrations due to the load application, while the remaining vibrations for the GC formulation do not affect the free vibration response, as discussed in Section 3.4.2. Importantly, the CP formulation returns better contact stress distributions, as shown in Section 3.4.4. Therefore, the CP formulation is preferable for our numerical model, and it is exclusively used for the discussion in Section 4.

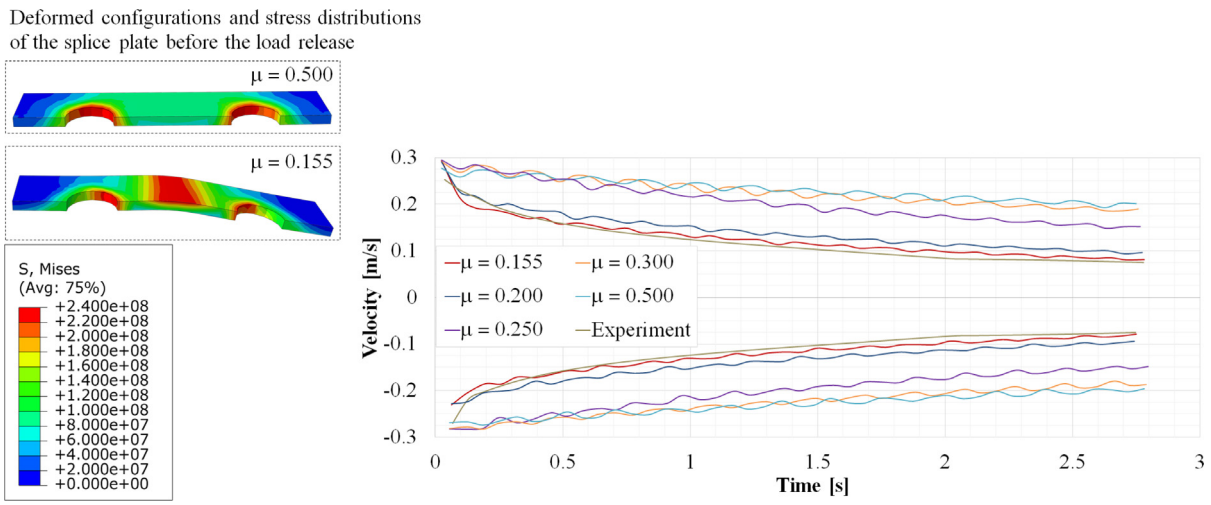

Fig. 27. Bolted beam splice connection and 100% of tightening force. Velocity time histories for different values of the friction coefficient. Deformed configurations and stress distributions in the upper flange are shown for $\mu = 0.155$ and $\mu = 0.500$, at the instance before the load release.

4. Discussion

In this section, we summarized and discuss the main results, and we scrutinize the nonlinear energy dissipation mechanism of the numerical model.

To properly describe experimental tests, the numerical model must be deliberately calibrated and verified, see Section 3.4. In a search for an optimal numerical model with respect to the efficiency and accuracy, mass scaling is one of the crucial parameters that requires calibration. An increase in the mass of a system can significantly improve the efficiency of explicit integration, but one must be careful about its effects on the accuracy. A careful verification presented in Section 3.4.3 shows that the adopted mass scaling approach does not induce large fictitious inertial forces but does manage to significantly increase the time step. Another important parameter of the numerical model is the order of numerical integration. The reduced integration of the C3D8R elements introduces the numerical damping that is practically equal to the material damping of our model. Regarding the contact formulations, both of them return the same velocity time histories but different stress distributions.

Besides the verification, the validation is another crucial step that tells us if the numerical model is aligned with the physics of a problem. The adopted numerical model is validated through the comparison of the experimental and numerical velocity time histories in Section 3.2.2. The experimental and numerical results for the BBSC100 model are in agreement, which is one of remarkable achievements of our study. Also, the correspondence of the results from the BBSC50 and BBSC30 models is satisfactory, considering the complexity of these models and their responses. In the rest of this section, we will focus on the BBSC100 model, since it is the one that is readily found in engineering structures.

The most important result of this research is the successful numerical modeling of structural damping due to friction in the BBSC model. Friction is a complicated phenomenon that depends on various parameters, as discussed in Section 1. In the adopted numerical model, friction is introduced via the classic Coulomb's law. This simplified approach is not an accurate representation of friction, but it returns an acceptable approximation. In order to scrutinize the influence of friction on the response of the BBSC100 model, we considered five simulations with different values of the friction coefficient, and the velocity envelopes are shown in Fig. 27. The model with $\mu = 0.155$ agrees with the experiment, as has already been discussed. Moreover, the experimental results are reasonably well aligned with the numerical model that has $\mu = 0.2$, which is actually the value that Eurocode recommends for non-treated steel surfaces [85]. A possible explanation for the lower value of friction that is found in our model is high air humidity, see Sections 1 and 2.2.1. Next, the structural response for $\mu = 0.25$ significantly differs, and the nonlinear damping effect almost vanishes. For the friction coefficients $\mu = 0.3$ and $\mu = 0.5$, the results are similar and the response is practically linear. Furthermore, our simulations show that the response of the BBSC model with $\mu > 0.3$ is practically identical to that of the WBSC model, which confirms our assumption, cf. Section 2.2.1. In contrast to the adopted numerical model with $\mu = 0.155$, the initial macro slip and the bending of the flange splice plate do not occur if the friction is considerable. This is evident from the stress distributions in the upper flange splice plate for $\mu = 0.155$ and $\mu = 0.500$, Fig. 27.

The friction coefficient strongly influences the local contact state. Actually, the nonlinear dynamic response is mainly caused by the friction between interacting contact surfaces. In general, we can distinguish between three types of relative motion between contacting surfaces: macro slip, stick, and micro slip. The macro slip occurs when the slip zone extends across the whole contact interaction and the relative displacement between all of the contact point pairs becomes similar. The stick state is characterized with near-zero relative displacement. The micro slip can be considered as a transitional state between the macro slip and stick states. This transition does not occur instantaneously, causing the stick and slip areas to exist at the same time. The micro-slipping ends after the whole contact interface turns into stick or macro slip. As discussed in Sections 1 and 2.2.3, the activation of micro- and macro-slipping depends on bolt forces and external excitation. With the reduction of the bolt tightening force, the slip region expands until it is active across the whole interface, defining the macro slip state. A case with a strong tightening force and a low excitation force will not result in slipping, as discussed in [2]. Such a situation corresponds to our previously analyzed case of $\mu > 0.3$.

To get further insight into the contact interaction of the considered beam, let us observe the upper part of the splice connection and three characteristic contact interfaces: the bolt head/washer, washer/splice plate, and splice plate/flange. The normal contact stress distributions at these interfaces, before the load release, are given in Fig. 28. The maximum contact stresses arise in the middle of the washer due to the stress concentration caused by the bolt head edge. Also, large contact stresses develop around the edges of the bolt holes and bolt heads, and they are concentrated towards the middle of the splice plate. Such a distribution is caused by the bending of the splice plate due to the initial macro-slipping.

The deformed configuration in Fig. 28 clearly illustrates that the initial macro slip occurred at the splice plate/flange interface. In order to scrutinize further this slip mechanism after the load release, let us observe the time history of slipping at the selected points. The points

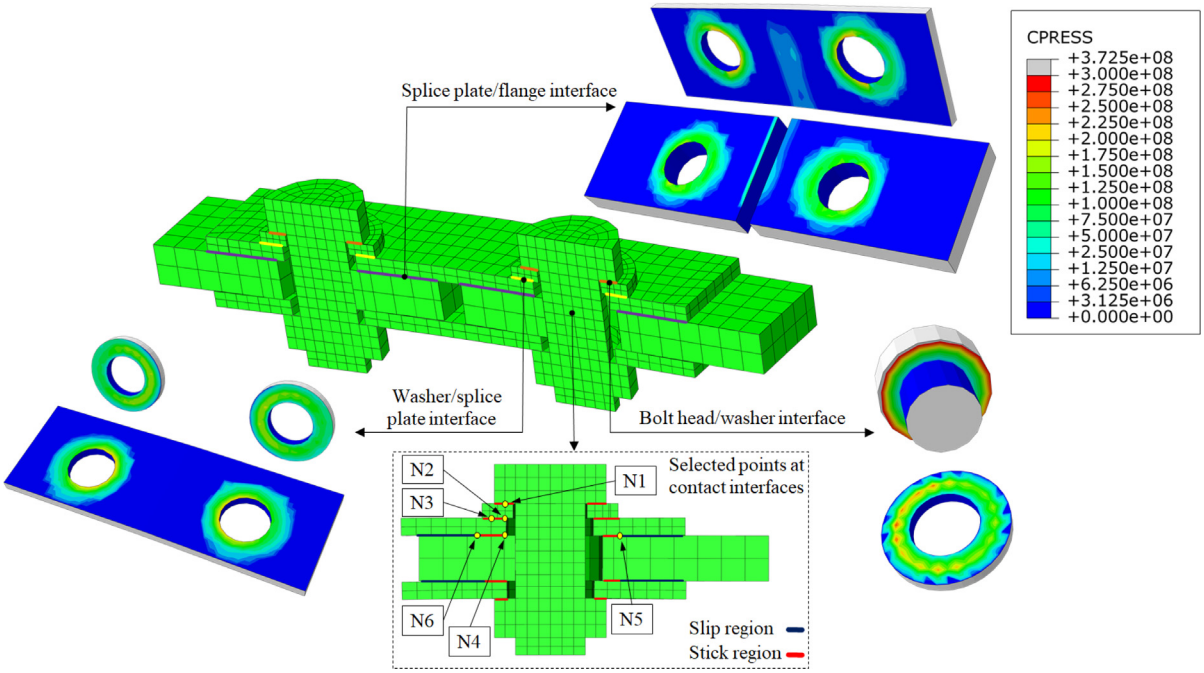

Fig. 28. Deformed configuration of the upper part of the splice connection before the load release. The normal contact stress distributions at the contact interfaces: bolt head/washer, washer/splice plate, and splice plate/flange. Six characteristic interacting contact point pairs are designated with N1-N6.

N1-N4 are selected near the areas with maximum contact stress where the stick state is expected. The points N5 and N6 are defined in the regions with reduced contact stress, symmetrical to the bolt hole, where the slip state is anticipated, Fig. 28. The slipping between the surfaces at a point is defined as the relative displacement between the two interacting points.

The time history of the relative displacement at point N5 is shown in the lower part of Fig. 29. Additionally, we calculated and plotted the differences between two consecutive amplitudes of opposite signs for all selected points. These graphs represent the envelopes of the estimated slip amplitudes. The relative displacement at the point N5 oscillates around approximately 1.05 mm, which is the value of relative static displacement due to the initial macro slip. The first slip amplitude at this point is 43 μm, and it sharply reduces to 11.6 μm during the next cycle. After a few more oscillations, the decay rate of slip amplitudes reaches a constant value. It is evident that similar behavior occurs at point N6.

After the first two slip amplitudes, the behavior at points N1-N4 is quite similar, although the values at points N1 and N2 are significantly lower. This sharp difference exists due to the maximum contact stresses in the vicinity of points N1 and N2. Nevertheless, the calculated slip amplitudes at points N1-N4 are less than 0.5 μm, which suggests that all of these points are practically in the stick state.

The slip at point N4 is the most intriguing. This point belongs to the same splice plate/flange contact interface as points N5 and N6. All three points have similar first amplitude of slip, which suggests the initial uniform displacement between the splice plate and the flange. This behavior corresponds to the macro slip state. Between the first and the third amplitude, the slip at point N4 reduces approximately by a factor of 60 and practically vanishes afterward. On the other hand, the slip amplitudes at points N5 and N6 decay at a lower rate. Therefore, the slips at points N5 and N6 monotonically decay, while the slip abruptly goes to the stick at point N4. This simultaneous presence of the stick and slip zones at the same contact interface is a clear indicator of the micro slip state.

To summarize, we can distinguish between three phases of slipping in our numerical simulations of the BBSC. The first phase consists of the slipping along the splice plate/flange interface during the application of mass M2. This is the initial macro slip and has an approximate amplitude of 1 mm. The second phase occurs immediately after the load release. Again, it consists of the macro-slipping at the splice plate/flange interface but its amplitude is significantly lower than the initial macro slip, approximately 40 μm. Finally, during the third phase, the stick zone forms at the splice plate/flange interface near the bolt shank, while the slipping is still present farther away from this region. This micro-slipping mechanism is the main cause of nonlinear energy dissipation in mechanical connections. As the energy dissipates from the system, the stick region grows steadily until the whole BBSC becomes practically monolithic.

5. Conclusions

We deliberately conducted in-depth experimental and numerical analyses of one bolted beam splice connection (BBSC). The carefully-designed experimental setup has shown a highly nonlinear dynamic response due to structural damping. The Abaqus/Explicit numerical model of the BBSC was verified and adopted through an iterative process, while the monolithic beam with welded connection was utilized for the initial calibration. We considered the influences of various parameters, such as time and spatial integration, bolt load application, load function, element type, contact formulation, bulk viscosity, and mass scaling. After the verification, the numerical model was successfully validated by the comparison with experimental data.

The main conclusions of the presented research are:

- Structural damping is a nonlinear phenomenon that is caused by the complex micro slip state at the contact interfaces of various joints, such as the commonly used bolted beam splice connections. The modeling of structural damping requires a well-designed experimental setup and precise post-processing of the measured data. These must be followed by a careful calibration, verification, and validation of the numerical model.
- When properly utilized, Abaqus/Explicit is a powerful tool for nonlinear dynamic simulations of structures with bolted connections. The non-physical parameters that require calibration and verification are the FE mesh, mass scaling, spatial and time integration schemes, and contact discretization.

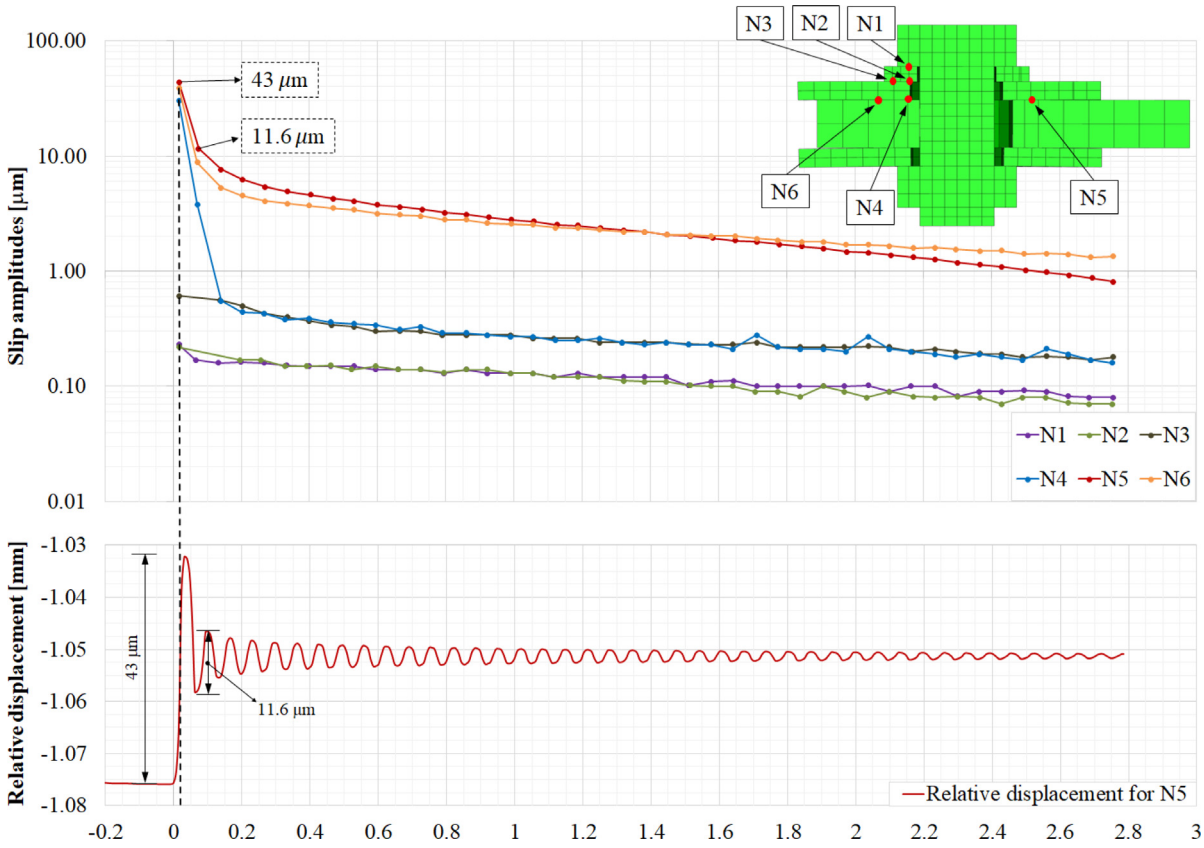

Fig. 29. Relative displacement between the characteristic points that are in the contact interaction. Lower figure shows the time history at point N5, while the upper figure gives differences between the consecutive amplitudes of opposite sign for all considered points - slip amplitudes.

- Proper calibration of the numerical model with respect to non-physical parameters allows us to assess the influence of main physical quantities. When the bolt tightening forces are given, one just has to adopt the loading function and the friction coefficient.
- For the adopted numerical model, the friction coefficient is near $\mu = 0.155$, which matches the values reported in the literature. The numerical and experimental results are in excellent correspondence for the case with 100% of the bolt tightening force, while the agreement of the results slightly deteriorates with a reduction of the bolt force. Nevertheless, the adopted numerical model predicts nonlinear structural damping with reasonably high accuracy.
- Engineering joints are complex, and their proper detailed numerical modeling is still inefficient for real-life calculations. This fact is the driving force for the development of accurate and efficient models that can provide approximate relations between essential engineering parameters, such as contact stresses, friction, and damping.

Finally, let us summarize some recommendations for the modeling of bolted connections in Abaqus/Explicit: (i) the contact pair formulation is the preferred option for the contact discretization, cf. Section 3.3.2, (ii) the additional mass should be applied by a smoothly increasing function, cf. Section 3.4.2, (iii) mass scaling is a crucial step that must be implemented with particular care, cf. Section 3.4.3, (iv) a numerical damping generated by the model should be estimated, cf. Section 3.4.4, (v) the quality of results must be verified by considering the model's energies, cf. Section 3.4.5, (vi) an influence of bulk viscosity on both stress and kinematic fields should be assessed, cf. Section 3.4.4.

The main limit of our research is its focus on one specific structural connection. As a recommendation for future work, it would be valuable to conduct a similar experiment and to test the mentioned observations regarding the calibration of the numerical model through a detailed parametric analysis. The geometry, position, and number of connections, and boundary conditions are parameters that should be taken into further consideration. The experiment should include a slip-resistant connection with various compositions of high-strength bolts, where influences of the roughness, oxidation, and lubrication would be scrutinized. Moreover, it is desirable to improve the quality of obtained data by using strain gauges and more accelerometers. These results will prove essential for modeling the energy dissipation in overall structures.

CRediT authorship contribution statement

O. Mijatović: Writing – original draft, Visualization, Validation, Supervision, Resources, Project administration, Methodology, Investigation, Funding acquisition, Formal analysis, Data curation, Conceptualization. **A. Borković:** Writing – original draft, Visualization, Validation, Supervision, Methodology, Investigation, Funding acquisition, Formal analysis, Data curation, Conceptualization. **M. Guzijan-Dilber:** Writing – original draft, Visualization, Validation, Methodology, Investigation, Formal analysis, Data curation. **Z. Mišković:** Supervision, Methodology, Investigation, Funding acquisition, Data curation. **R. Salatić:** Supervision, Methodology, Investigation, Funding acquisition, Data curation. **R. Mandić:** Supervision, Methodology, Formal analysis. **V. Golubović-Bugarski:** Validation, Project administration, Methodology, Funding acquisition, Data curation.

Declaration of competing interest

The authors declare that they have no known competing financial interests or personal relationships that could have appeared to influence the work reported in this paper.

Data availability

Data will be made available on request.

Acknowledgments

A. Borković acknowledges the support of the Austrian Science Fund (FWF): P 36019-N.

References

[1] K.L. Johnson, Contact Mechanics, Cambridge University Press, Cambridge, ISBN: 978-0-521-34796-9, 1985, http://dx.doi.org/10.1017/CBO9781139171731.
[2] M.R.W. Brake (Ed.), The Mechanics of Jointed Structures: Recent Research and Open Challenges for Developing Predictive Models for Structural Dynamics, first ed. 2018 ed., Springer, New York, NY, ISBN: 978-3-319-56816-4, 2017.
[3] D. Segalman, J. Lauffer, M. Jew, D. Gregory, M. Starr, B. Resor, N. Ames, Handbook on dynamics of jointed structures, Tech. rep., 2009, 1028891, http://dx.doi.org/10.2172/1028891, SAND2009–4164.
[4] Department for Business, Innovation and Skills, Airbus in the UK, A400M Wing Assembly at the Manufacturing Facility at Airbus Filton, Bristol, 2010, https://www.flickr.com/photos/bisgovuk/7158201628/.
[5] Cblade, Turbine Blades for Steam Turbine and Gas Turbine Compressor, 2009, https://commons.wikimedia.org/wiki/File:TurbineBlades.jpg.
[6] L. Pesaresi, L. Salles, A. Jones, J.S. Green, C.W. Schwingshackl, Modelling the nonlinear behaviour of an underplatform damper test rig for turbine applications, Mech. Syst. Signal Process. 85 (2017) 662–679, http://dx.doi.org/10.1016/j.ymssp.2016.09.007.
[7] I.A. Sever, E.P. Petrov, D.J. Ewins, Experimental and numerical investigation of rotating bladed disk forced response using underplatform friction dampers, J. Eng. Gas Turbines Power 130 (4) (2008) http://dx.doi.org/10.1115/1.2903845.
[8] H.-T. Thai, T.P. Vo, T.-K. Nguyen, C.H. Pham, Explicit simulation of bolted endplate composite beam-to-CFST column connections, Thin-Walled Struct. 119 (2017) 749–759, http://dx.doi.org/10.1016/j.tws.2017.07.013.
[9] H. Liu, X. Liu, Z. Chen, Y. Ouyang, J. Yin, Mechanical properties of bolted connections for aluminum alloy structures at elevated temperatures, Thin-Walled Struct. 157 (2020) 107067, http://dx.doi.org/10.1016/j.tws.2020.107067.
[10] K. Jiang, K.H. Tan, O. Zhao, Net section fracture of S700 high strength steel staggered bolted connections, Thin-Walled Struct. 164 (2021) 107904, http://dx.doi.org/10.1016/j.tws.2021.107904.
[11] M. Groper, Microslip and macroslip in bolted joints, Exp. Mech. 25 (2) (1985) 171–174, http://dx.doi.org/10.1007/BF02328808.
[12] R.N. Hopkins, L.A.A. Heitman, A method to capture macroslip at bolted interfaces, in: M. Allen, R.L. Mayes, D. Rixen (Eds.), Dynamics of Coupled Structures, in: Conference Proceedings of the Society for Experimental Mechanics Series, vol. 4, Springer International Publishing, Cham, ISBN: 978-3-319-29763-7, 2016, pp. 213–229, http://dx.doi.org/10.1007/978-3-319-29763-7_21.
[13] L. Gaul, J. Lenz, Nonlinear dynamics of structures assembled by bolted joints, Acta Mech. 125 (1) (1997) 169–181, http://dx.doi.org/10.1007/BF01177306.
[14] E. Popova, V.L. Popov, The research works of Coulomb and Amontons and generalized laws of friction, Friction 3 (2) (2015) 183–190, http://dx.doi.org/10.1007/s40544-015-0074-6.
[15] M. A. Chowdhury, D. M. Nuruzzaman, M. Arefin Kowser, M. MostafizurRahman, B. K. Roy, S. Chakraborty, M. Didarul Islam, M. Aktaruzzaman, N. Mohammad, Sliding friction of steel combinations, Open Mech. Eng. J. 8 (1) (2014) 364–369, http://dx.doi.org/10.2174/1874155X01408010364.
[16] E. Rabinowicz, Friction and Wear of Materials, second ed., Wiley-Interscience, New York, ISBN: 978-0-471-83084-9, 1995.
[17] F.P. Bowden, D. Tabor, The Friction and Lubrication of Solids, Revised ed., Oxford University Press, Oxford : New York, ISBN: 978-0-19-850777-2, 2001.
[18] I. Nitta, Measurements of Real Contact Areas using PET films (thickness, 0.9 Mm), 10th International Conference on Wear of Materials, Wear 181–183 (1995) 844–849, http://dx.doi.org/10.1016/0043-1648(95)90205-8.
[19] V.A. Yastrebov, G. Anciaux, J.-F. Molinari, From infinitesimal to full contact between rough surfaces: Evolution of the contact area, Int. J. Solids Struct. 52 (2015) 83–102, http://dx.doi.org/10.1016/j.ijsolstr.2014.09.019.
[20] M. Eguchi, T. Shibamiya, T. Yamamoto, Measurement of Real Contact Area and analysis of stick/slip region, Special Issue: 35th Leeds-Lyon Symposium, Tribol. Int. 42 (11) (2009) 1781–1791, http://dx.doi.org/10.1016/j.triboint.2009.04.046.
[21] J.A. Greenwood, J.B.P. Williamson, Contact of Nominally Flat Surfaces, Proc. R. Soc. A 295 (1442) (1966) 300–319.
[22] J.A. Greenwood, K.L. Johnson, E. Matsubara, A surface roughness parameter in Hertz contact, Wear 100 (1) (1984) 47–57, http://dx.doi.org/10.1016/0043-1648(84)90005-X.
[23] B.N.J. Persson, Theory of rubber friction and contact mechanics, J. Chem. Phys. 115 (8) (2001) 3840–3861, http://dx.doi.org/10.1063/1.1388626.
[24] P. Wriggers, Computational Contact Mechanics, second ed., Springer, Berlin ; New York, ISBN: 978-3-540-32608-3, 2006.
[25] V. Yastrebov, Computational Contact Mechanics: Geometry, Detection and Numerical Techniques, 2011.
[26] S. Bettscheider, C. Gachot, A. Rosenkranz, How to measure the Real Contact Area? A simple marker and relocation foot-printing approach, Tribol. Int. 103 (2016) 167–175, http://dx.doi.org/10.1016/j.triboint.2016.06.034.
[27] J.F. Archard, Elastic deformation and the laws of friction, Proc. R. Soc. A 243 (1233) (1957) 190–205.
[28] G. Carbone, F. Bottiglione, Contact mechanics of rough surfaces: A comparison between theories, Meccanica 46 (3) (2011) 557–565, http://dx.doi.org/10.1007/s11012-010-9315-y.
[29] J.R. Barber, Multiscale surfaces and amontons' law of friction, Tribol. Lett.s 49 (3) (2013) 539–543, http://dx.doi.org/10.1007/s11249-012-0094-6.
[30] M.H. Müser, W.B. Dapp, R. Bugnicourt, P. Sainsot, N. Lesaffre, T.A. Lubrecht, B.N.J. Persson, K. Harris, A. Bennett, K. Schulze, S. Rohde, P. Ifju, W.G. Sawyer, T. Angelini, H. Ashtari Esfahani, M. Kadkhodaei, S. Akbarzadeh, J.-J. Wu, G. Vorlaufer, A. Vernes, S. Solhjoo, A.I. Vakis, R.L. Jackson, Y. Xu, J. Streator, A. Rostami, D. Dini, S. Medina, G. Carbone, F. Bottiglione, L. Afferrante, J. Monti, L. Pastewka, M.O. Robbins, J.A. Greenwood, Meeting the contact-mechanics challenge, Tribol. Lett. 65 (4) (2017) 118, http://dx.doi.org/10.1007/s11249-017-0900-2.
[31] V.A. Yastrebov, J. Durand, H. Proudhon, G. Cailletaud, Rough surface contact analysis by means of the Finite Element Method and of a new reduced model, Surface Mechanics : Facts and Numerical Models, Comptes Rendus Mécanique 339 (7) (2011) 473–490, http://dx.doi.org/10.1016/j.crme.2011.05.006.
[32] J. Han, J. Zhu, W. Zheng, G. Wang, Influence of metal forming parameters on surface roughness and establishment of surface roughness prediction model, Int. J. Mech. Sci. 163 (2019) http://dx.doi.org/10.1016/j.ijmecsci.2019.105093.
[33] A.I. Vakis, V.A. Yastrebov, J. Scheibert, L. Nicola, D. Dini, C. Minfray, A. Almqvist, M. Paggi, S. Lee, G. Limbert, J.F. Molinari, G. Anciaux, R. Aghababaei, S. Echeverri Restrepo, A. Papangelo, A. Cammarata, P. Nicolini, C. Putignano, G. Carbone, S. Stupkiewicz, J. Lengiewicz, G. Costagliola, F. Bosia, R. Guarino, N.M. Pugno, M.H. Müser, M. Ciavarella, Modeling and simulation in tribology across scales: An overview, Tribol. Int. 125 (2018) 169–199, http://dx.doi.org/10.1016/j.triboint.2018.02.005.
[34] I. Singer, H. Pollock, Fundamentals of Friction: Macroscopic and Microscopic Processes, vol. 220, ISBN: 978-0-7923-1912-2, 1992, http://dx.doi.org/10.1007/978-94-011-2811-7,
[35] M.S. Bonney, B.A. Robertson, M. Mignolet, F. Schempp, M.R. Brake, Experimental determination of frictional interface models, in: M. Allen, R.L. Mayes, D. Rixen (Eds.), Dynamics of Coupled Structures, in: Conference Proceedings of the Society for Experimental Mechanics Series, vol. 4, Springer International Publishing, Cham, ISBN: 978-3-319-29763-7, 2016, pp. 473–490, http://dx.doi.org/10.1007/978-3-319-29763-7_47.
[36] A. Fantetti, L.R. Tamatam, M. Volvert, I. Lawal, L. Liu, L. Salles, M.R.W. Brake, C. Schwingshackl, D. Nowell, The impact of fretting wear on structural dynamics: Experiment and Simulation, Tribol. Int. 138 (2019) 111–124, http://dx.doi.org/10.1016/j.triboint.2019.05.023.
[37] P.J. Blau, Four great challenges confronting our understanding and modeling of sliding friction, in: D. Dowson, C.M. Taylor, T.H.C. Childs, G. Dalmaz, Y. Berthier, L. Flamand, J.M. Georges, A.A. Lubrecht (Eds.), Tribology Series, in: Tribology for Energy Conservation, vol. 34, Elsevier, 1998, pp. 117–128, http://dx.doi.org/10.1016/S0167-8922(98)80067-9.
[38] F.P. Bowden, D. Tabor, Mechanism of metallic friction, Nature 150 (3798) (1942) 197–199, http://dx.doi.org/10.1038/150197a0.
[39] M.A. Chowdhury, M.M. Helali, The effect of frequency of vibration and humidity on the coefficient of friction, Tribol. Int. 39 (9) (2006) 958–962, http://dx.doi.org/10.1016/j.triboint.2005.10.002.
[40] W.Y.H. Liew, Effect of relative humidity on the unlubricated wear of metals, Wear 260 (7) (2006) 720–727, http://dx.doi.org/10.1016/j.wear.2005.04.011.
[41] P.J. Blau, Friction Science and Technology: From Concepts To Applications, second ed., CRC Press, Boca Raton, ISBN: 978-0-429-13711-2, 2008, http://dx.doi.org/10.1201/9781420054101.
[42] D. Tabor, Friction—The present state of our understanding, J. Lubr. Technol. 103 (2) (1981) 169–179, http://dx.doi.org/10.1115/1.3251622.
[43] M.D. Pashley, J.B. Pethica, D. Tabor, Adhesion and micromechanical properties of metal surfaces, Wear 100 (1) (1984) 7–31, http://dx.doi.org/10.1016/0043-1648(84)90003-6.
[44] J.S. McFarlane, D. Tabor, F.P. Bowden, Relation between friction and adhesion, Proc. R. Soc. A 202 (1069) (1950) 244–253, http://dx.doi.org/10.1098/rspa.1950.0097.
[45] G.W. Stachowiak, A.W. Batchelor, Engineering Tribology, third ed., Butterworth-Heinemann, Amsterdam ; Boston, ISBN: 978-0-7506-7836-0, 2005.
[46] S. Venkatesan, D.A. Rigney, Sliding friction and wear of plain carbon steels in air and vacuum, Wear 153 (1) (1992) 163–178, http://dx.doi.org/10.1016/0043-1648(92)90268-D.
[47] F.P. Bowden, G.W. Rowe, The adhesion of clean metals, Proc. R. Soc. A 233 (1195) (1956) 429–442, http://dx.doi.org/10.1098/rspa.1956.0001.

[48] P.L. Menezes, M. Nosonovsky, S.P. Ingole, S.V. Kailas, M.R. Lovell, Tribology for Scientists and Engineers: From Basics to Advanced Concepts, Springer Science & Business Media, ISBN: 978-1-4614-1945-7, 2013.

[49] M.J. Furey, Surface temperatures in sliding contact, A S L E Trans. 7 (2) (1964) 133–146, http://dx.doi.org/10.1080/05698196408972043.

[50] Y. Waddad, V. Magnier, P. Dufrénoy, G. De Saxcé, Heat partition and surface temperature in sliding contact systems of rough surfaces, Int. J. Heat Mass Transfer 137 (2019) 1167–1182, http://dx.doi.org/10.1016/j.ijheatmasstransfer.2019.04.015.

[51] W. Qin, X. Jin, A. Kirk, P.H. Shipway, W. Sun, Effects of surface roughness on local friction and temperature distributions in a steel-on-steel fretting contact, Tribol. Int. 120 (2018) 350–357, http://dx.doi.org/10.1016/j.triboint.2018.01.016.

[52] C.W. Schwingshackl, E.P. Petrov, D.J. Ewins, Measured and estimated friction interface parameters in a nonlinear dynamic analysis, Interdisciplinary and Integration Aspects in Structural Health Monitoring, Mech. Syst. Signal Process. 28 (2012) 574–584, http://dx.doi.org/10.1016/j.ymssp.2011.10.005.

[53] D.L. Goldsby, T.E. Tullis, Flash heating leads to low frictional strength of crustal rocks at earthquake slip rates, Science 334 (6053) (2011) 216–218, http://dx.doi.org/10.1126/science.1207902.

[54] H.R. Le, M.P.F. Sutcliffe, J.A. Williams, Friction and material transfer in micro-scale sliding contact between aluminium alloy and steel, Tribol. Lett. 18 (1) (2005) 99–104, http://dx.doi.org/10.1007/s11249-004-1762-y.

[55] S. Rohm, M. Hasler, C. Knoflach, J. van Putten, S.H. Unterberger, K. Schindelwig, R. Lackner, W. Nachbauer, Friction between steel and snow in dependence of the steel roughness, Tribol. Lett. 59 (1) (2015) 27, http://dx.doi.org/10.1007/s11249-015-0554-x.

[56] Y. Meng, J. Xu, Z. Jin, B. Prakash, Y. Hu, A review of recent advances in tribology, Friction 8 (2) (2020) 221–300, http://dx.doi.org/10.1007/s40544-020-0367-2.

[57] T. Mang (Ed.), Encyclopedia of lubricants and lubrication, 2014th ed., Springer, New York, ISBN: 978-3-642-22646-5, 2014.

[58] C.V. Madhusudana, Thermal Contact Conductance, in: Mechanical Engineering Series, Springer International Publishing, Cham, ISBN: 978-3-319-01275-9, 2014, http://dx.doi.org/10.1007/978-3-319-01276-6.

[59] B.N.J. Persson, E. Tosatti (Eds.), Physics of Sliding Friction, 1996th ed., Springer, Dordrecht ; Boston, ISBN: 978-0-7923-3935-9, 1996.

[60] E.E. Ungar, Energy Dissipation at Structural Joints; Mechanisms and Magnitudes, Tech. rep., 1964, AD0607257.

[61] E.E. Ungar, The status of engineering knowledge concerning the damping of built-up structures, J. Sound Vib. 26 (1) (1973) 141–154, http://dx.doi.org/10.1016/S0022-460X(73)80210-X.

[62] C. Hartwigsen, Y. Song, D. McFarland, L. Bergman, A. Vakakis, Experimental study of non-linear effects in a typical shear lap joint configuration, J. Sound Vib. 277 (1–2) (2004) 327–351, http://dx.doi.org/10.1016/j.jsv.2003.09.018.

[63] H.G.D. Goyder, D.P.T. Lancereau, P. Ind, D. Brown, Friction and damping associated with bolted joints: Results and signal processing, in: Proceedings of the ISMA 2016 International Conference on Noise and Vibration Engineering, Leuven, 2016, p. 11.

[64] L. Gaul, R. Nitsche, The role of friction in mechanical joints, Appl. Mech. Rev. 54 (2) (2001) 93–106, http://dx.doi.org/10.1115/1.3097294.

[65] C. Li, X. Miao, R. Qiao, Q. Tang, Modeling method of bolted joints with micro-slip features and its application in flanged cylindrical shell, Thin-Walled Struct. 164 (2021) 107854, http://dx.doi.org/10.1016/j.tws.2021.107854.

[66] D. Segalman, An Initial Overview of Iwan Modeling for Mechanical Joints, Tech. rep., (SAND2001-0811) 2001, 780307, http://dx.doi.org/10.2172/780307.

[67] W.D. Iwan, On a class of models for the yielding behavior of continuous and composite systems, J. Appl. Mech. 34 (3) (1967) 612–617, http://dx.doi.org/10.1115/1.3607751.

[68] D.J. Segalman, A four-parameter Iwan model for lap-type joints, J. Appl. Mech. 72 (5) (2005) 752–760, http://dx.doi.org/10.1115/1.1989354.

[69] B.J. Deaner, M.S. Allen, M.J. Starr, D.J. Segalman, Investigation of modal Iwan models for structures with bolted joints, in: R. Mayes, D. Rixen, M. Allen (Eds.), Topics in Experimental Dynamic Substructuring, in: Conference Proceedings of the Society for Experimental Mechanics Series, vol. 2, Springer, New York, NY, ISBN: 978-1-4614-6540-9, 2014, pp. 9–25, http://dx.doi.org/10.1007/978-1-4614-6540-9_2.

[70] D. Roettgen, M.S. Allen, D. Kammer, R.L. Mayes, Substructuring of a non-linear beam using a modal Iwan framework, Part I: Nonlinear modal model identification, in: M.S. Allen, R.L. Mayes, D.J. Rixen (Eds.), Dynamics of Coupled Structures, in: Conference Proceedings of the Society for Experimental Mechanics Series, vol. 4, Springer International Publishing, Cham, ISBN: 978-3-319-54930-9, 2017, pp. 165–178, http://dx.doi.org/10.1007/978-3-319-54930-9_15.

[71] J.R. Barber, Contact Mechanics, Springer, ISBN: 978-3-319-70939-0, 2018.

[72] A. Konyukhov, R. Izi, Introduction To Computational Contact Mechanics: A Geometrical Approach, first ed., Wiley, Chichester, West Sussex, ISBN: 978-1-118-77065-8, 2015.

[73] O. Mijatović, Z. Mišković, R. Salatić, R. Mandić, V. Golubović-Bugarski, G. Relja, Experimental analysis of structural damping for bolted and welded splice connection joint for IPE-80 steel profile, Int. Conf. Contemp. Theory Pract. Constr. (14) (2020) http://dx.doi.org/10.7251/STP2014032M.

[74] O. Mijatović, R. Salatić, Z. Mišković, V. Golubović-Bugarski, M. Guzjan-Dilber, N. Lujić, Numerical and experimental anaysis of structural damping for bolted splice connection joint, J. Faculty Civil Eng. 37 (2021) 297–307, http://dx.doi.org/10.14415/konferencijaGFS2021.28.

[75] T. Diehl, D. Carroll, B. Nagaraj, Applications of DSP to explicit dynamic FEA simulations of elastically-dominated impact problems, Shock Vib. 7 (3) (2000) 167–177, http://dx.doi.org/10.1155/2000/931351.

[76] T.S. Edwards, Effects of aliasing on numerical integration, Mech. Syst. Signal Process. 21 (1) (2007) 165–176, http://dx.doi.org/10.1016/j.ymssp.2005.08.009.

[77] Getting Started with ABAQUS/Explicit: Keywords Version (v6.5-1). https://classes.engineering.wustl.edu/2009/spring/mase5513/abaqus/docs/v6.5.

[78] L. Fasanella, K.E. Jackson, Best Practices for Crash Modeling and Simulation, Tech. rep., (NASA/TM-2002-211944) 2002, p. 99.

[79] ABAQUS. User's Manual, Version 6.14, Dassault Systemes Corp., Providence, RI, USA, 2014.

[80] R.J. Boulbes, Troubleshooting Finite-Element Modeling with Abaqus: With Application in Structural Engineering Analysis, first ed. 2020 ed., Springer, Cham, ISBN: 978-3-030-26739-1, 2019.

[81] L. Carlotta Pagnini, G. Solari, Damping measurements of steel poles and tubular towers, Eng. Struct. 23 (9) (2001) 1085–1095, http://dx.doi.org/10.1016/S0141-0296(01)00011-6.

[82] M.C. Moynihan, J.M. Allwood, Utilization of structural steel in buildings, Proc. R. Soc. A 470 (2168) (2014) 20140170, http://dx.doi.org/10.1098/rspa.2014.0170.

[83] C.F. Dunant, M.P. Drewniok, S. Eleftheriadis, J.M. Cullen, J.M. Allwood, Regularity and optimisation practice in steel structural frames in real design cases, Resour. Conserv. Recy. 134 (2018) 294–302, http://dx.doi.org/10.1016/j.resconrec.2018.01.009.

[84] J.-P. Jaspart, K. Weynand, Design of Joints in Steel Structures: Eurocode 3: Design of Steel Structures; Part 1-8 Design of Joints, first ed., Ernst & Sohn, ISBN: 978-3-433-60871-5, 2017.

[85] I. Vayas, J. Ermopoulos, G. Ioannidis, Design of Steel Structures To Eurocodes, Springer International Publishing, ISBN: 978-3-319-95473-8, 2018.

[86] F. Magalhães, Á. Cunha, E. Caetano, R. Brincker, Damping estimation using free decays and ambient vibration tests, Special Issue: Operational Modal Analysis, Mech. Syst. Signal Process. 24 (5) (2010) 1274–1290, http://dx.doi.org/10.1016/j.ymssp.2009.02.011.

[87] P. Avitabile, Modal Testing: A Practitioner's Guide, first ed., Wiley, Hoboken, NJ, ISBN: 978-1-119-22289-7, 2017.

[88] R. Brincker, C.E. Ventura, P. Andersen, Damping estimation by frequency domain decomposition, in: Proceedings of IMAC 19, Society for Experimental Mechanics, 2001, pp. 698–703.

[89] A. Cunha, E. Caetano, R. Delgado, Dynamic tests on large cable-stayed bridge, J. Bridge Eng. 6 (1) (2001) 54–62, http://dx.doi.org/10.1061/(ASCE)1084-0702(2001)6:1(54).

[90] R. Stafford, Cumulative Cubic Integration , MATLAB Central File Exchange, 2022, https://Www.Mathworks.Com/Matlabcentral/Fileexchange/19152-Cumulative-Cubic-Integration. Retrieved August 29, 2022.

[91] H. Goyder, P. Ind, D. Brown, Development of a Method for Measuring Damping in Bolted Joints, 2011, http://dx.doi.org/10.1115/DETC2011-47230.

[92] H. Goyder, P. Ind, D. Brown, Measurement of damping in bolted joints, in: ASME 2012 International Design Engineering Technical Conferences and Computers and Information in Engineering Conference, American Society of Mechanical Engineers Digital Collection, 2013, pp. 399–408, http://dx.doi.org/10.1115/DETC2012-70896.

[93] Optimization Toolbox User's Guide, R2016b, 2016, The MathWorks, Inc. 3 Apple Hill Drive Natick, MA 01760-2098.

[94] Z. Ugray, L. Lasdon, J. Plummer, F. Glover, J. Kelly, R. Martí, Scatter search and local NLP solvers: A multistart framework for global optimization, INFORMS J. Comput. 19 (3) (2007) 328–340, http://dx.doi.org/10.1287/ijoc.1060.0175.

[95] G. Dinger, C. Friedrich, Avoiding self-loosening failure of bolted joints with numerical assessment of local contact state, Eng. Fail. Anal. 18 (8) (2011) 2188–2200, http://dx.doi.org/10.1016/j.engfailanal.2011.07.012.

[96] W. Chen, X. Deng, Structural damping caused by micro-slip along frictional interfaces, Int. J. Mech. Sci. 47 (8) (2005) 1191–1211, http://dx.doi.org/10.1016/j.ijmecsci.2005.04.005.

[97] H. Wentzel, M. Olsson, Mechanisms of dissipation in frictional joints - influence of sharp contact edges and plastic deformation, Wear 265 (11) (2008) 1814–1819, http://dx.doi.org/10.1016/j.wear.2008.04.026.

[98] M. Pavlović, C. Heistermann, M. Veljković, D. Pak, M. Feldmann, C. Rebelo, L. Simões da Silva, Friction connection vs. Ring flange connection in steel towers for wind converters, Eng. Struct. 98 (2015) 151–162, http://dx.doi.org/10.1016/j.engstruct.2015.04.026.

[99] B. Egan, C.T. McCarthy, M.A. McCarthy, P.J. Gray, R.M. Frizzell, Modelling a single-bolt countersunk composite joint using implicit and explicit finite element analysis, Proceedings of the 21st International Workshop on Computational Mechanics of Materials (IWCMM 21), Comput. Mater. Sci. 64 (2012) 203–208, http://dx.doi.org/10.1016/j.commatsci.2012.02.008.

[100] M.A. McCarthy, C.T. McCarthy, V.P. Lawlor, W.F. Stanley, Three-dimensional finite element analysis of single-bolt, single-lap composite bolted joints: Part I—model development and validation, Compos. Struct. 71 (2) (2005) 140–158, http://dx.doi.org/10.1016/j.compstruct.2004.09.024.

[101] J. VonNeumann, R.D. Richtmyer, A method for the numerical calculation of hydrodynamic shocks, J. Appl. Phys. 21 (3) (1950) 232–237, http://dx.doi.org/10.1063/1.1699639.

[102] L. Mahéo, V. Grolleau, G. Rio, Numerical damping of spurious oscillations: A comparison between the bulk viscosity method and the explicit dissipative Tchamwa-Wielgosz scheme, Comput. Mech. 51 (1) (2013) 109–128, http://dx.doi.org/10.1007/s00466-012-0708-8.

[103] T. Belytschko, J.S.-J. Ong, W.K. Liu, J.M. Kennedy, Hourglass control in linear and nonlinear problems, Comput. Methods Appl. Mech. Engrg. 43 (3) (1984) 251–276, http://dx.doi.org/10.1016/0045-7825(84)90067-7.

[104] D.P. Flanagan, T. Belytschko, A uniform strain hexahedron and quadrilateral with orthogonal hourglass control, Internat. J. Numer. Methods Engrg. 17 (5) (1981) 679–706, http://dx.doi.org/10.1002/nme.1620170504.

[105] I. LSTC, G. DYNAmore, Total Energy, LS-DYNA Support, 2022, http://www.dynasupport.com/howtos/general/total-energy. Accessed August 29, 2022.

[106] G. Zheng, H. Nie, J. Chen, C. Chen, H.P. Lee, Dynamic analysis of lunar lander during soft landing using explicit finite element method, Acta Astronaut. 148 (2018) 69–81, http://dx.doi.org/10.1016/j.actaastro.2018.04.014.

[107] Z.-H. Zhong, Finite Element Procedures for Contact-Impact Problems, Oxford University Press, Oxford, New York, ISBN: 978-0-19-856383-9, 1993.

[108] N. Jakšić, K.-F. Nilsson, Numerical simulation of one metre drop test on bar for CASTOR cask, Packag. Transp. Storage Secur. Radioact. Mater. 19 (3) (2008) 142–150, http://dx.doi.org/10.1179/174651008X344430.